

Annual and interannual variations of the Leeuwin Current at 32°S

Ming Feng,¹ Gary Meyers,² Alan Pearce,¹ and Susan Wijffels²

Received 23 December 2002; revised 31 August 2003; accepted 12 September 2003; published 18 November 2003.

[1] In this study, the annual and interannual variations of the Leeuwin Current at 32°S off the Western Australian coast are investigated. The mean annual cycle and the El Niño and La Niña composites of the Leeuwin Current temperature structures are obtained by linearly fitting a Taylor expansion to historical upper ocean temperature data. A temperature-salinity relationship is used to derive the salinity field and geostrophy is assumed to calculate the current velocity. The downward tilting of the isotherms toward the coast and the strength of a near-surface core of the low-salinity water indicate the seasonal variation of the Leeuwin Current. Seasonally, the Leeuwin Current has the maximum poleward geostrophic transport of 5 Sv ($10^6 \text{ m}^3 \text{ s}^{-1}$) during June–July. Interannually, the Leeuwin Current is distinctly stronger during a La Niña year and weaker during an El Niño year. The annual average poleward geostrophic transports in the mean, the El Niño and La Niña years are 3.4, 3.0, and 4.2 Sv respectively. Variations of the Leeuwin Current structure on annual and interannual timescales are coastally trapped. A linear relationship between the coastal sea level deviation at Fremantle and the Leeuwin Current transport is derived, which justifies and calibrates the usage of the Fremantle sea level as an index for the strength of the Leeuwin Current.

INDEX TERMS: 4516

Oceanography: Physical: Eastern boundary currents; 4522 Oceanography: Physical: El Niño; 4556

Oceanography: Physical: Sea level variations; 4572 Oceanography: Physical: Upper ocean processes;

KEYWORDS: Leeuwin Current, annual cycle, ENSO, Fremantle sea level, XBT

Citation: Feng, M., G. Meyers, A. Pearce, and S. Wijffels, Annual and interannual variations of the Leeuwin Current at 32°S, *J. Geophys. Res.*, 108(C11), 3355, doi:10.1029/2002JC001763, 2003.

1. Introduction

[2] The dominant surface ocean current off the Western Australian coast in the Southeast Indian Ocean is the southward-flowing Leeuwin Current [Cresswell and Golding, 1980] (Figure 1). An anomalously large meridional pressure gradient, set up by the warm, low-density tropical Pacific Ocean water entering the Indian Ocean through the Indonesian Archipelago [e.g., Meyers *et al.*, 1995; Feng and Wijffels, 2002], is believed to account for the existence of the Leeuwin Current [Thompson, 1984, 1987; Godfrey and Ridgway, 1985; McCreary *et al.*, 1986; Weaver and Middleton, 1989; Batteen and Rutherford, 1990]. The pressure gradient drives an eastward, onshore geostrophic transport, which overwhelms local wind-driven offshore Ekman transport and feeds the Leeuwin Current.

[3] The Leeuwin Current is a narrow and meandering current near the continental shelf break, which brings low-salinity, warm tropical waters poleward along the Western Australian coast [Pearce, 1991; Smith *et al.*, 1991]. Early studies indicated that the current is stronger during austral winter, with a southward volume transport up to 5 Sv ($10^6 \text{ m}^3 \text{ s}^{-1}$) [Smith *et al.*, 1991]. The annual cycle is

suggested to be mostly due to variations in the northward wind stress, which is stronger during the austral summer [McCreary *et al.*, 1986; Kundu and McCreary, 1986; Smith *et al.*, 1991]. Some studies suggest that annual variation of the meridional pressure gradient at the shelf break may also contribute [Godfrey and Ridgway, 1985; Morrow and Birol, 1998]. During the austral summer, the increased northward wind stress also drives the northward Capes Current on the continental shelf [Cresswell *et al.*, 1989; Pearce and Pattiaratchi, 1999].

[4] The El Niño/Southern Oscillation (ENSO) related interannual signals propagate poleward along the northwest to western Australian coast as coastally trapped waves [Clarke and Liu, 1994; Meyers, 1996; Wijffels and Meyers, 2003]. Along the coastal waveguide illustrated in Figure 1, the waves transmit high coastal sea levels during the La Niña years and low sea levels during the El Niño years [Pariwono *et al.*, 1986]. The correlation between the Southern Oscillation Index and Fremantle sea level was found to be 0.73 during 1968–1986 [Pearce and Phillips, 1988]. The ENSO-relationship is further demonstrated in the correlations between regional altimeter sea level anomalies and the Southern Oscillation index (SOI) for the years 1992–2002 (Figure 2). The correlations are generally 0.6–0.7 along the northwest and west Australian coast.

[5] There is a growing need to understand the annual and interannual variability of the Leeuwin Current and their impacts on regional climate, marine ecosystems, and fisheries. A potentially important climate link for southwestern

¹CSIRO Marine Research, Floreat, Western Australia, Australia.

²CSIRO Marine Research, Hobart, Tasmania, Australia.

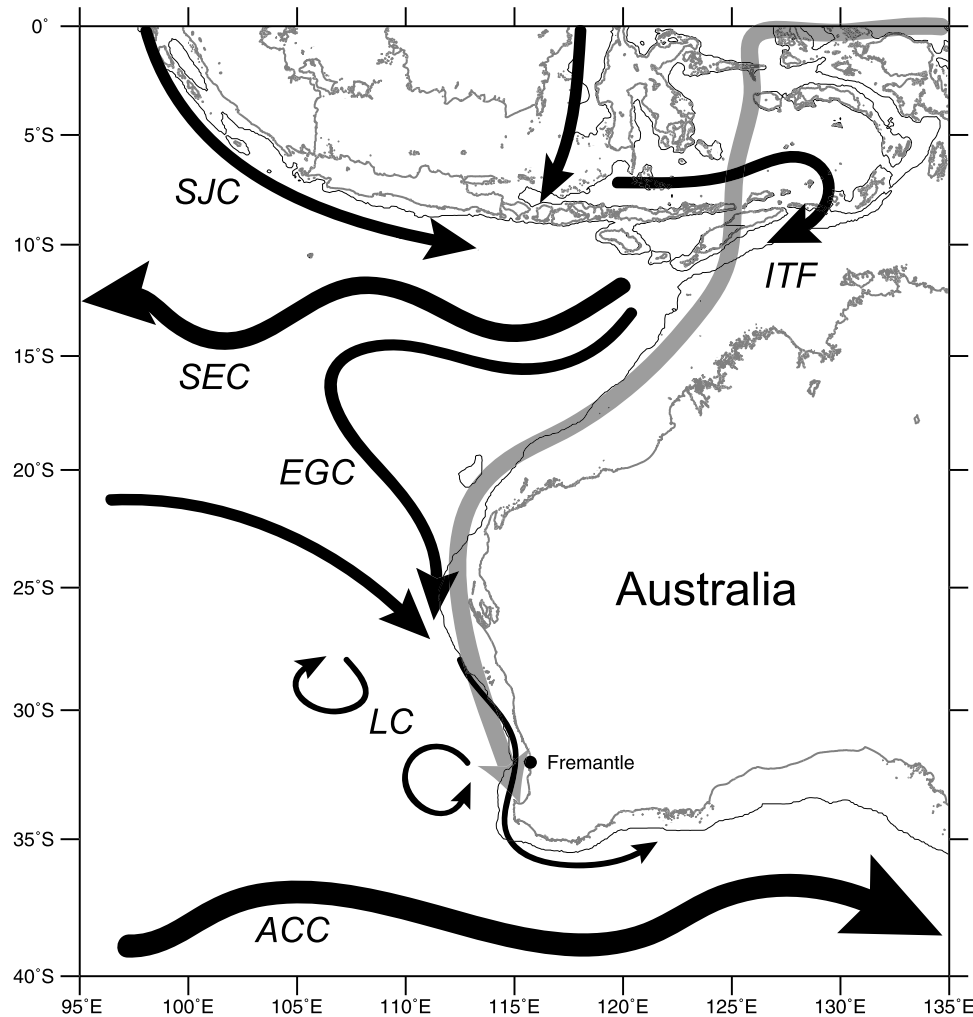


Figure 1. Schematic of the major surface currents in the east-southeast Indian Ocean. ITF: Indonesian Throughflow; SEC: South Equatorial Current; SJC: South Java Current; EGC: East Gyral Current; LC: Leeuwin Current; ACC: Antarctic Circumpolar Current. The meandering of the SEC and the Leeuwin Current eddies are also sketched. A shaded, transparent arrow is used to highlight the waveguide along which the Pacific ENSO signals propagate. The 1000-m bathymetry is shown. See color version of this figure in the HTML.

Australia is the southward advection of warm water by the Leeuwin Current [Godfrey and Ridgway, 1985; Pearce, 1991]. The average sea surface temperature (SST) off Australia's west coast near 32°S is 20.8°C, which is 5.6 and 4.2°C higher than those at the same latitude near the eastern boundaries in the Pacific and Atlantic Oceans (Table 1). Correspondingly, the precipitation rate in the coastal area of southwest Australia is more than twice the precipitation rates in southwest South America and Africa (Table 1). This demonstrates the potential impact of the Leeuwin Current on the coastal climate in southwest Western Australia.

[6] Pearce and Phillips [1988] hypothesized that coastal sea level at Fremantle could be a proxy for the Leeuwin Current strength, so that the current is stronger during La Niña years and weaker during El Niño years. Interannual variability of the Fremantle sea level is highly correlated to the recruitment to a number of local fisheries, including the western rock lobster [Pearce and Phillips, 1988; Griffin et al., 2001],

Australia's most valuable single species fishery, so that the Fremantle sea level is widely used in fishery recruitment research to represent the Leeuwin Current strength [Caputi et al., 1995]. Still, the relationship between the Fremantle sea level and the Leeuwin Current needs to be established, as a first step to understand how the Leeuwin Current variability affects ecosystem processes and fisheries recruitment.

[7] The present study examines the annual and ENSO-related interannual Leeuwin Current variations derived from historical upper ocean thermal data, and verifies and calibrates the Fremantle sea level index in terms of surface current strength and geostrophic transport. The correlations between the Fremantle and altimeter sea level anomalies are high along the coast (Figure 2), which suggests that the Fremantle sea level index may apply to a large geographic range of the Leeuwin Current although the calibration to the current strength will vary with location.

[8] The organization of the paper is as follows. In section 2, we introduce the data used in this study. In section 3, we

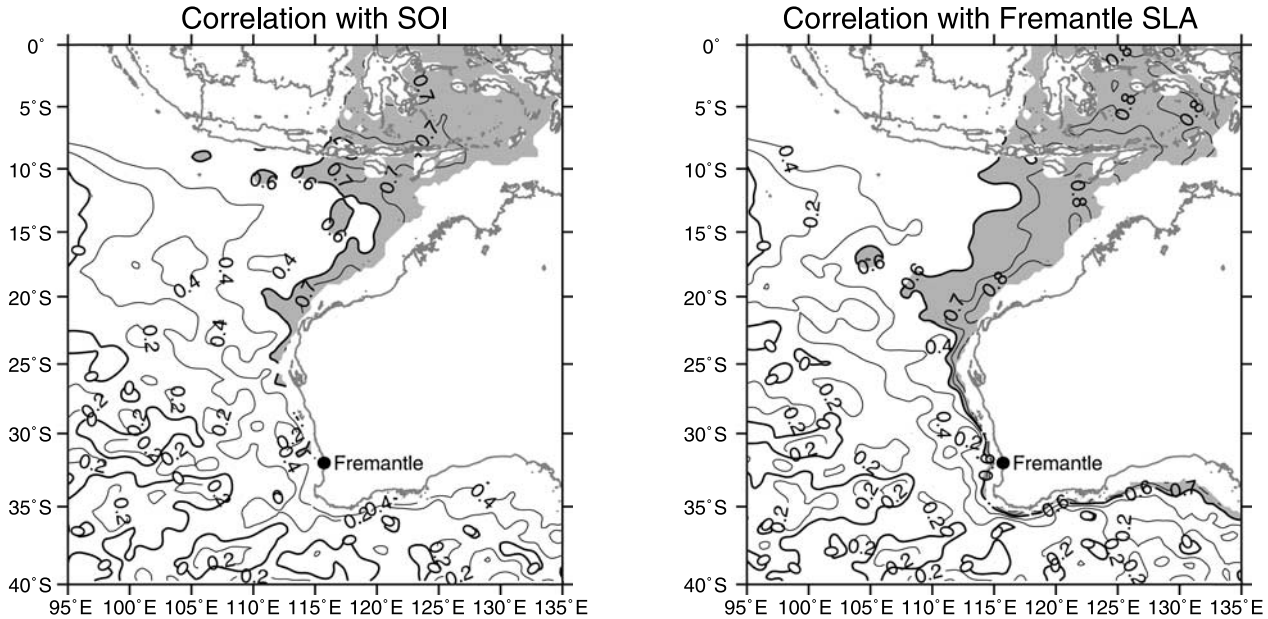


Figure 2. Correlations between the satellite altimeter monthly sea level anomaly in the east-southeast Indian Ocean and the (left) SOI and the (right) Fremantle sea level anomaly. Shadings denote correlations higher than 0.6. See color version of this figure in the HTML.

present the method to construct the seasonal climatology from the upper ocean thermal archive. The results for the annual climatology and ENSO composites are presented and compared with the Fremantle sea level variations in sections 4 and 5, respectively. In section 6, we discuss and summarize the results. In the Appendices, we establish the dynamic balance in the Leewin Current to support the analysis and carry out some sensitivity tests for the methodology of constructing the upper ocean climatology.

2. Data

[9] The data used in this study are monthly Fremantle sea level records obtained from the National Tidal Facility in Adelaide, mean sea level pressure from the National Center for Environment Prediction (NCEP) [Kalnay et al., 1996], upper ocean temperature data off Fremantle from the Indian Ocean Thermal Archive (IOTA) of CSIRO Marine Research (A. Gronell et al., manuscript in preparation, 2003), the mean and annual harmonics of the temperature-salinity relationship [Dunn and Ridgway, 2002], temperature and salinity records at a hydrographical station west of Rottnest Island [Rochford, 1988], and the Southern Oscillation Index (SOI) from the Bureau of Meteorology, Australia. All data are from 1950 to 2000, when the Fremantle sea level record has the best continuity. We also use the Southampton Oceanography Centre (SOC) surface air-sea flux climatology [Josey et al., 1999]. The bathymetry is taken from the National Geophysical Data Center 2-min resolution product [Smith and Sandwell, 1997], and the coastline from the Global Self-Consistent, Hierarchical, High-Resolution Shoreline database [Wessel and Smith, 1996].

[10] Fremantle ($32^{\circ}03'S$, $115^{\circ}44'E$) is a major port in the southeast Indian Ocean (Figure 3). Sea level has been recorded at Fremantle since the port was opened in 1897. South of Fremantle, there is a semi-enclosed embayment,

Cockburn Sound, of about 20 m depth and 10 km in size [D'Adamo, 2002]. Rottnest Island ($32^{\circ}S$, $115^{\circ}30'E$) is about 18 km to the west of Fremantle (Figure 3). Thus Fremantle harbour faces the open ocean mostly to the north. The continental shelf off Rottnest Island is very narrow; the 200-m isobath is only about 20 km seaward of the island (Figure 4). A submarine canyon extends from the deep ocean toward the island (Figure 3), which is hypothesized to be a main feeding ground for the blue whales sighted in the area. The meandering nature of the submarine canyon is shown in the bottom topography along $32^{\circ}S$ (Figure 4).

[11] Monthly Fremantle sea level deviation is calculated by removing the 1950 to 2000 mean and applying a 1-2-1 weighted 3-month moving average. The anomaly field, or sea level anomaly (SLA), is then obtained by removing the average annual cycle from the sea level deviation (note the difference between sea level deviation and SLA). Monthly sea level atmospheric pressure is taken from the closest grid point to Fremantle in the NCEP data. Similarly, after removing the 1950–2000 average and applying the same 3-month moving average, the atmospheric pressure data are used to apply the inverted barometric correction to the Fremantle sea level deviation [Reid and Mantyla, 1976].

Table 1. Annual Mean Sea Surface Temperatures (SST) and Precipitation Rates Near $32^{\circ}S$ at the West Coast of the Three Continents

	Australia	South America	Africa
SST, $^{\circ}C^a$	20.8	15.2	16.6
Precipitation, $mm\ day^{-1}^b$	1.8	0.8	0.8

^aThe SST is taken from the Levitus and Boyer [1994] temperature climatology.

^bThe mean precipitation rate is taken from the Merged Analysis of Precipitation (CMAP) data averaged between 1978 and 2000 [Xie and Arkin, 1997].

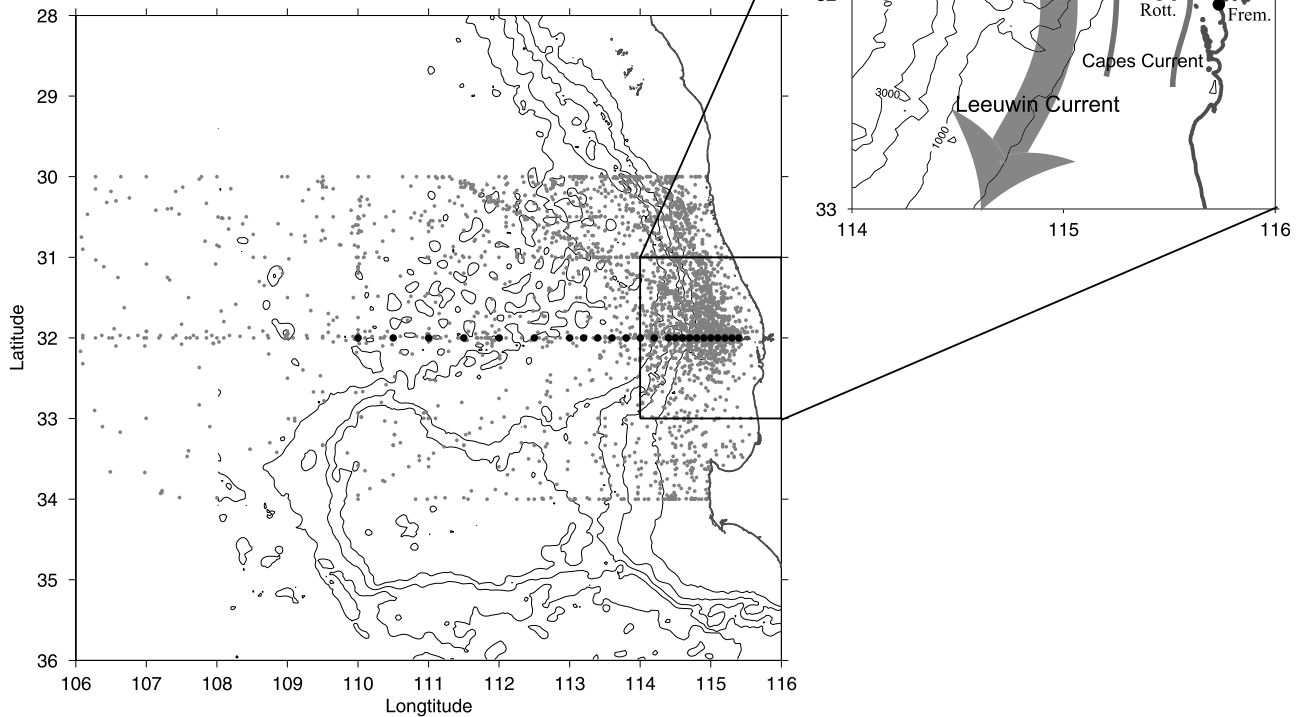


Figure 3. Locations of historical temperature profiles collected off Fremantle, Western Australia, during 1950–2000. The black dots along 32°S are the grid points where the upper ocean climatology was calculated. The bottom topography is contoured every 1000 m. In the inset, the 300-m isopleth of bottom topography is added, and the locations of the Leeuwin Current and Capes Current are denoted. Rott: Rottnest Island; Frem: Fremantle.

As the atmospheric pressure increases and decreases, the sea surface is assumed to respond hydrostatically, that is, a 1 hPa increase in the atmospheric pressure depresses the sea surface by 1 cm. The corrected SLA is obtained by removing the average annual cycle from the corrected sea level deviation. Hereinafter, the Fremantle sea level deviation and SLA refer to the corrected sea level deviation and corrected SLA.

[12] Figure 3 shows the spatial distribution of temperature profiles taken during 1950–2000 which exist in the upper-ocean thermal archive. Only data between 30°S and 34°S and from 106°E to the coast are used in this study. While most profiles were collected near the commercial shipping lines off Fremantle, data density along 32°S is also relatively high due to research cruises. The thermal data were vertically interpolated to 5-m intervals and a semi-automatic screening process was applied for quality control (A. Gronell et al., manuscript in preparation, 2003). In this study, further editing is carried out to ensure that profiles with temperature inversions higher than 1°C are removed, and outliers with temperature anomalies higher than 3 standard deviations within 5° boxes are also

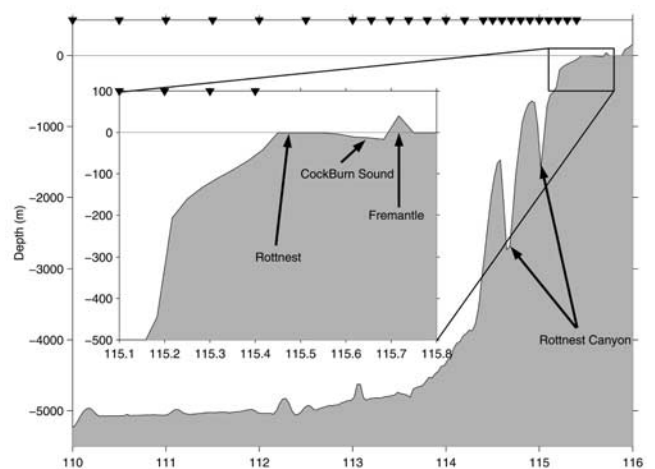


Figure 4. Bottom topography along 32°S . The inverted triangles mark the locations of the climatology grid points. The enlarged inset shows the approximate locations of Fremantle and Rottnest Island.

removed. After the editing, there is a total of 4443 casts in the region.

3. Construction of the Upper Ocean Climatology

[13] In this section, we present the technique used to construct the upper ocean climatology from the edited temperature data and a historic T-S relationship. The temperature climatology spans from 110°E to 115.4°E along 32°S, with increasing grid density toward the coast (Figure 3). The eastern-most grid point (32°S, 115.4°E) is in 55 m water depth, about 10 km west of Rottnest Island and close to the CSIRO Rottnest station [Rochford, 1988]. The grid resolution at the eastern end of the section is 0.1° in longitude.

[14] The temperature surrounding each horizontal ($x_0, y_0 = 32^\circ\text{S}$) and vertical (every 5 m from surface to 300 m) grid point, and centered in the middle of each month d_0 , is expressed with a Taylor expansion:

$$\begin{aligned} T_C(x, y, d, \text{SLA}) = & T_{C0} + T_x \times (x - x_0) + T_y \times (y - y_0) + T_d \\ & \times (d - d_0) + T_{\text{SLA}} \times \text{SLA} + c_1(x - x_0)^2 + c_2 \\ & \times (x - x_0)(y - y_0) + c_3(y - y_0)^2 + \varepsilon. \end{aligned}$$

Here x, y are longitude and latitude and d is observation day of year. The parameters are depth dependent: T_{C0} (the monthly mean temperature value at $x_0, y_0, d_0, \text{SLA} = 0$), T_x, T_y, T_d , and T_{SLA} (the linear gradients of temperature relative to longitude, latitude, day of year, and the Fremantle SLA), and c_1, c_2 and c_3 (parameters for second-order terms). Here ε represents the high-order residuals. To estimate the parameters, the expansion is fitted by the method of least squares to the observed temperatures within searching radii in time and space. The temporal searching radius is 1.5 months. The spatial searching domain is an ellipse with the meridional radius being 5 times the zonal radius. The zonal radius is variable between preset minimum and maximum radii, both decreasing toward the coast. The selection criterion of the zonal radius is to ensure that there are at least 40 observations in each fit. The fitting method is similar to the locally weighted least squares (LOESS) mapping tool [Cleveland and Devlin, 1988; Dunn and Ridgway, 2002]. Following Dunn and Ridgway [2002], a tri-cubic weighting function is used: $w = (1 - r^3)^3, 0 \leq r \leq 1$, where r is normalized with the searching radius and the topographic adjusted relief function (TAR) [Dunn and Ridgway, 2002].

[15] Because of the strong ENSO influence in this region, interannual variations are taken into account in the temperature fitting to avoid bias caused by uneven sampling in the ENSO cycle. This is accomplished by assigning the Fremantle SLA to each temperature profile based on the observation year and month, and treating the Fremantle SLA as an independent variable in the above temperature fitting. There are good linear correlations between the SOI and the satellite altimeter SLA along the Western Australian coast during 1992 to 2002 (Figure 2). However, the SOI has a jump in the mid-1970 because of the influence of a climate regime shift [Nitta and Yamada, 1989; Gershunov and Barnett, 1998], and the Fremantle SLA features a less abrupt response to this regime shift, as shown later in

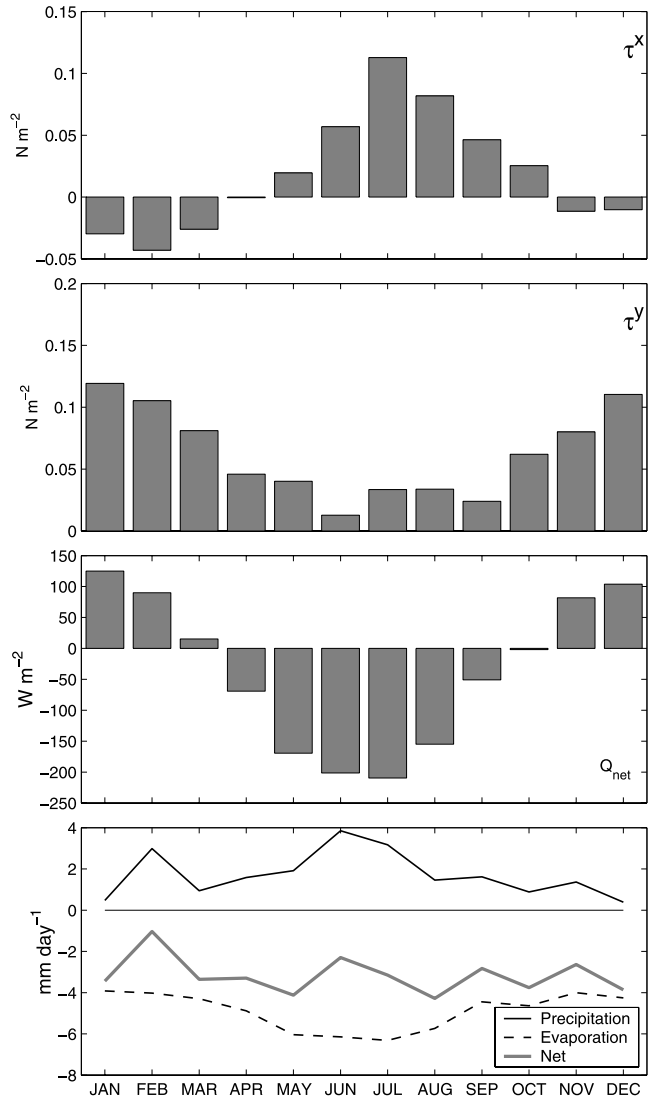


Figure 5. Monthly zonal and meridional wind stresses (τ^x, τ^y), net surface air-sea heat flux (Q_{net}), and freshwater flux at 32°S, 114.5°E from the SOC climatology.

section 5. Hence the relationship between the SOI and the Fremantle SLA (as well as the upper ocean temperature) over the multidecadal timescale is not linear. Thus we use a Taylor expansion of temperature relative to the Fremantle SLA instead of the SOI to represent the interannual variability. However, as shown in Appendix B3, the conclusions from this study can be similarly derived when we use the SOI to replace the Fremantle SLA in the temperature fit, with the consideration of the climate shift effect.

[16] The seasonal-varying temperature-salinity relationship product was obtained by fitting the historical salinity data on temperature surfaces with a mean and an annual harmonic (J. Dunn, personal communication, 2002). This product is used to derive the monthly mean T-S relationship and hence the salinity at our temperature climatology grids. The salinity for any out-of-range temperature is assigned with the closest value.

[17] From scale analysis, the poleward Leewin Current is in geostrophic balance (Appendix A). In calculating the

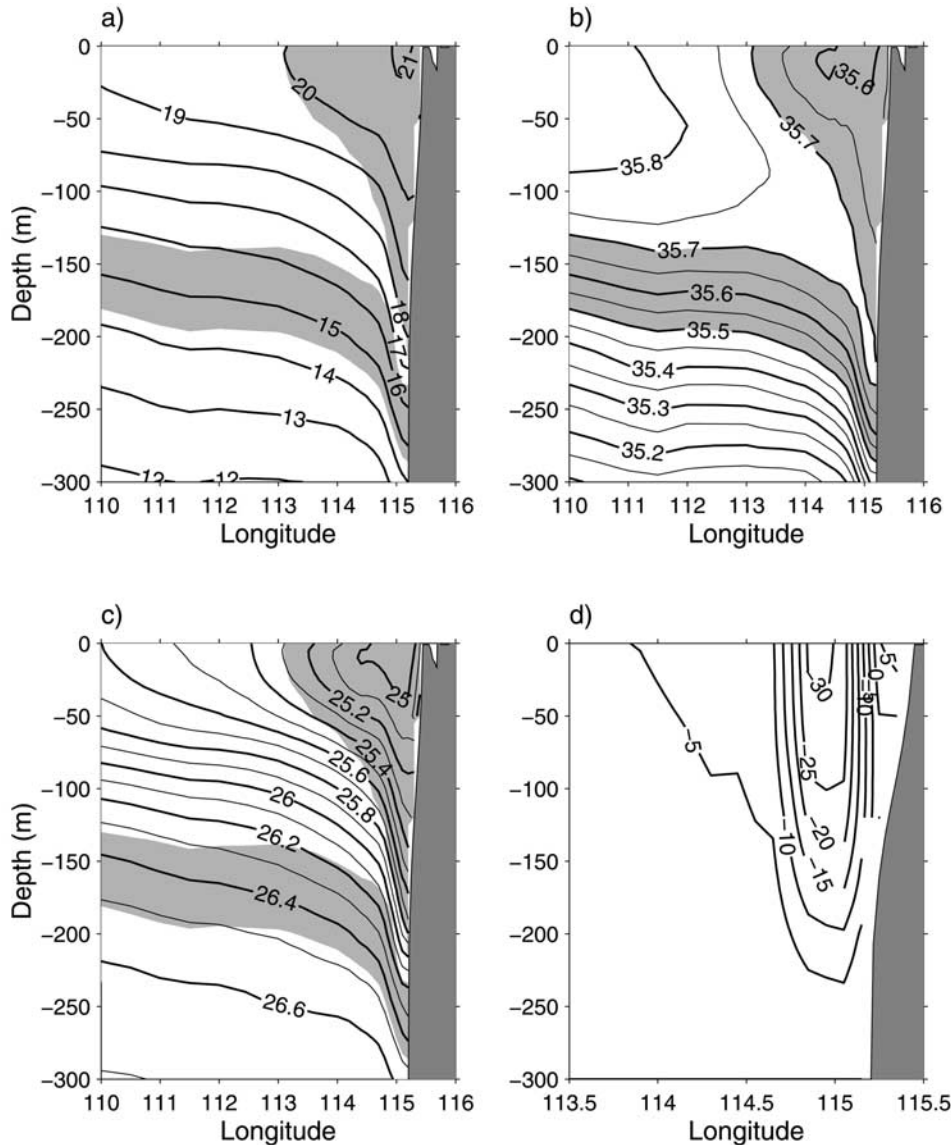


Figure 6. Mean (a) temperature, (b) salinity, (c) potential density, and (d) geostrophic current velocity along 32°S . The units are $^{\circ}\text{C}$, psu, kg m^{-3} , and cm s^{-1} , respectively. Shaded areas are with salinity between 35.5–35.7 psu. Note that the zonal range of the velocity plot is reduced.

geostrophic current velocity along 32°S , 300 m is used as a reference depth for the dynamic height [Smith *et al.*, 1991]. Two grid points along the section are shallower than 300 m (Figure 4). For these two grids, linear extrapolation of offshore dynamic height is used, following Reid and Mantyla [1976]. The northward undercurrent below 300 m [Thompson, 1984] will not be analyzed in this study.

[18] In Appendix B, we validate the upper ocean climatology using the Rottnest station data and carry out some sensitivity tests to ensure that the results are not strongly affected by the reference depth and other constraints we use.

4. Mean State and Annual Cycle

[19] In this section, we first examine the climatological surface air-sea fluxes at 32°S . Note that in the climatology these fluxes have larger spatial scale than the narrow Leeuwin Current. We then present the mean and annual

cycle of the Leeuwin Current structure at 32°S . Furthermore, we propose that the annual variation of the Leeuwin Current is coastally trapped and examine the relationship between the annual cycles of the Fremantle sea level and the inshore dynamic height.

4.1. Surface Air-Sea Fluxes

[20] The SOC climatology shows clear annual cycles in both the eastward and northward wind stress components off Fremantle (Figure 5). The annual mean zonal and meridional wind stresses are 0.02 and 0.06 N m^{-2} , respectively. The eastward wind stress is strongest during austral winter (reaching 0.11 N m^{-2} in July) and brings warm moist air inland to cause winter rainfall in southwest Western Australia. The wind is weakly westward between October and March. The meridional component of the wind is always northward, being stronger during austral summer with a maximum wind stress of 0.12 N m^{-2} in January.

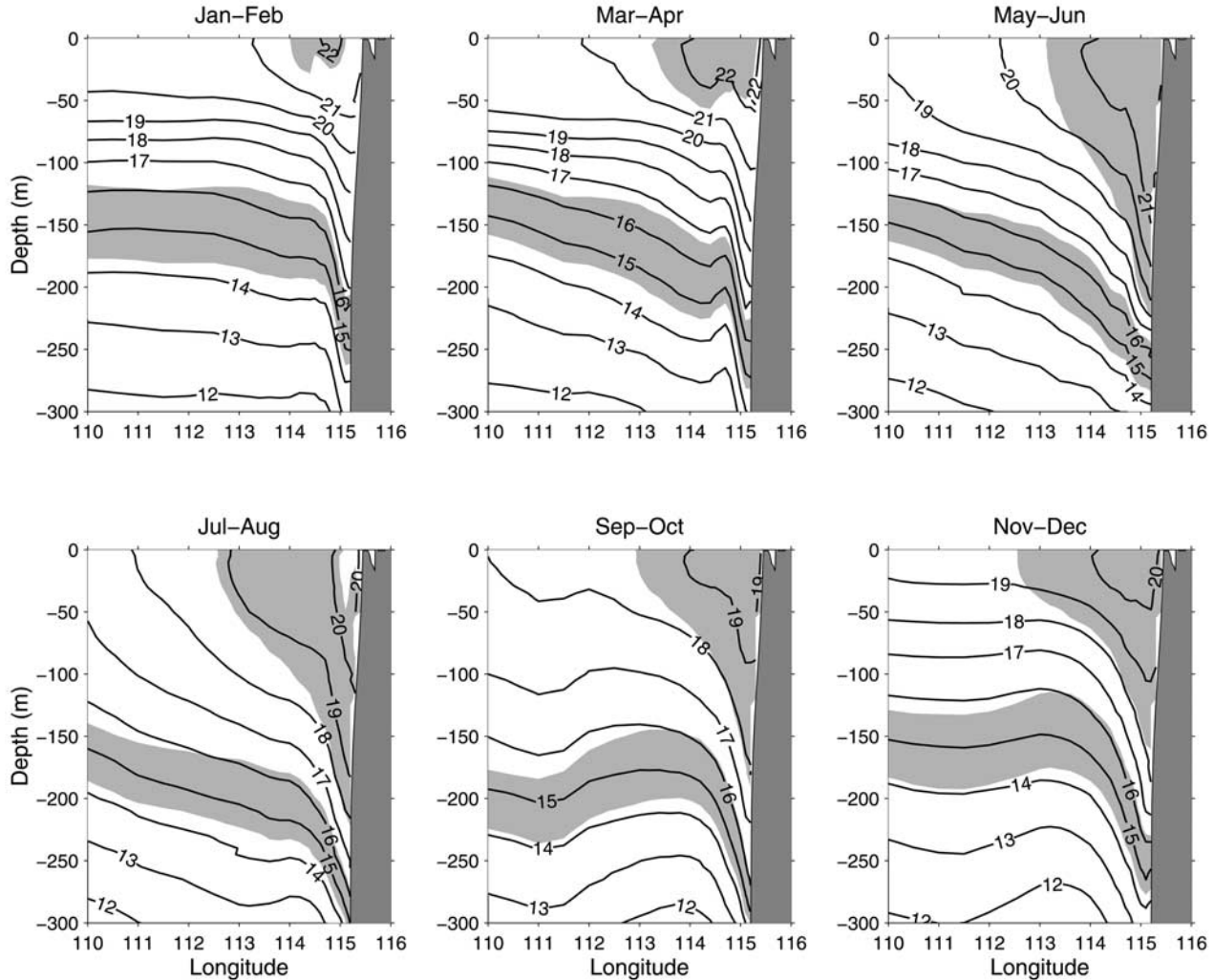


Figure 7. Bimonthly averages of the climatology (a) temperature, (b) salinity, and (c) geostrophic velocity along 32°S. The units are °C, psu, and cm s⁻¹ respectively. Shaded areas are with salinity between 35.5 and 35.7 psu. Note that the zonal range of the velocity plots is reduced.

[21] The SOC climatology also shows a distinct annual cycle of the net air-sea heat flux off Fremantle (Figure 5). The ocean gains heat between November and March, but has a stronger heat loss during the winter months. The heat loss is more than 200 W m⁻² in June–July, and the annual mean heat loss is 37 W m⁻². Evaporation is stronger than precipitation all year round. Both the precipitation and evaporation rates have maxima during the winter season, so that the net freshwater loss is about 2–4 mm day⁻¹ and has only a weak annual cycle.

4.2. Mean Structure of the Leewin Current

[22] The mean temperature, salinity, potential density, and geostrophic velocity derived from the climatology along 32°S (Figure 6) agree with earlier descriptions of the Leewin Current [Smith *et al.*, 1991]. The Leewin Current is characterized by surface water that is low in salinity, highlighted in Figure 6 with shading in the 35.5–35.7 psu salinity range. The shading delineates the near surface Leewin Current water adjacent to the coast, as well as the depth of the mid-thermocline (centered on the 15°–16°C isotherms).

[23] The temperature stratification (Figure 6a) determines the density and geostrophic current structures (Figures 6c and 6d). The deepening of the offshore high salinity tongue toward the coast (Figure 6b) suggests that the onshore geostrophic flow subducts with the outcropping isopycnals (Figure 6c). Salinity decreases with depth below the 16°C isotherm (Figure 6b), causing the weaker density stratification at depth (Figure 6c).

[24] Since the Leewin Current is a narrow current, only a sub-domain with strong geostrophic velocities referenced to 300 m is shown (Figure 6d). The core of the Leewin Current is located between 114.9°E–115°E, offshore of the 300-m isobath, with a peak southward velocity above 30 cm s⁻¹ at the sea surface. The velocity core tilts slightly toward the coast with increasing depth. The annual mean geostrophic transport east of 110°E is 3.4 Sv (10^6 m³ s⁻¹), while the annual mean Ekman transport across the section is only 0.1 Sv.

4.3. Mean Annual Cycle of the Leewin Current

[25] Bimonthly mean temperature, salinity, and geostrophic velocity fields along 32°S are presented to docu-

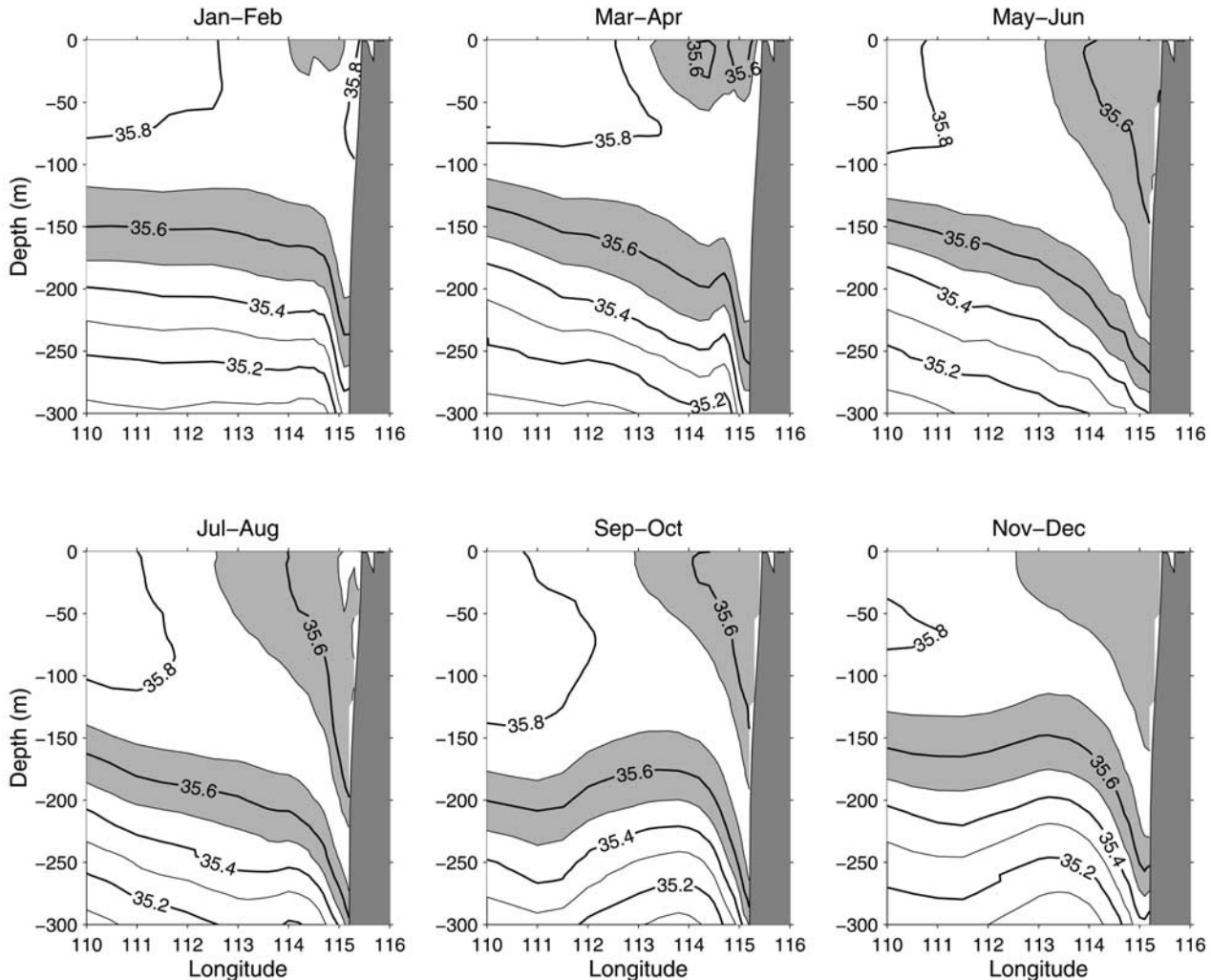


Figure 7. (continued)

ment the annual cycle of the Leeuwin Current (Figure 7). The near surface stratification is highly variable throughout the year (Figure 7a). A seasonal thermocline develops between 50 and 100 m from November through April, and the peak surface temperature reaches 22°C in March–April near the core of the Leeuwin Current. The seasonal thermocline starts to erode from May to June, with decreased surface layer temperature and outcropping deep isotherms. The variations induced by the stratification of the Leeuwin Current dominate during the other months. The tilting of isotherms in the thermocline, while confined near the coast during austral summer, becomes broader across the section during the winter months.

[26] During January–February when the Leeuwin Current is weak, the surface layer salinity is mostly above 35.7 psu (Figure 7b). The areas occupied by the near-surface low-salinity waters are indications of the strength variations of the Leeuwin Current. Freshening of the surface layer from January to June can only be due to strengthened freshwater advection by the Leeuwin Current because of the net freshwater loss at the air-sea interface. From September, the Leeuwin Current water starts to

become more saline, likely due to weaker freshwater advection compared to the surface freshwater loss and mixing.

[27] In the summer months, the geostrophic velocity is rather weak (Figure 7c), but a distinct Leeuwin Current is still present. The southward velocities of larger than 10 cm s^{-1} are centered at 115°E , with a width of less than 50 km. The Leeuwin Current starts to strengthen in March–April, forming a narrow jet with a peak velocity of 45 cm s^{-1} . During May–August, the Leeuwin Current broadens, with the 10 cm s^{-1} southward velocity extending to almost 114°E . The broadening of the current in May–August is associated with a secondary maximum offshore (Figure 7c). This could be related to eddy processes in the Leeuwin Current that are not completely random [Morrow and Birol, 1998], or are not adequately sampled by the upper ocean thermal archive data.

[28] Figure 8 shows the annual cycle of the geostrophic transport across the section east of 110°E . The transport is 2–3 Sv during the summer months. It starts to increase in March, peaks at about 5 Sv in June–July, and then begins to decrease in August. From the SOC climatology zonal wind

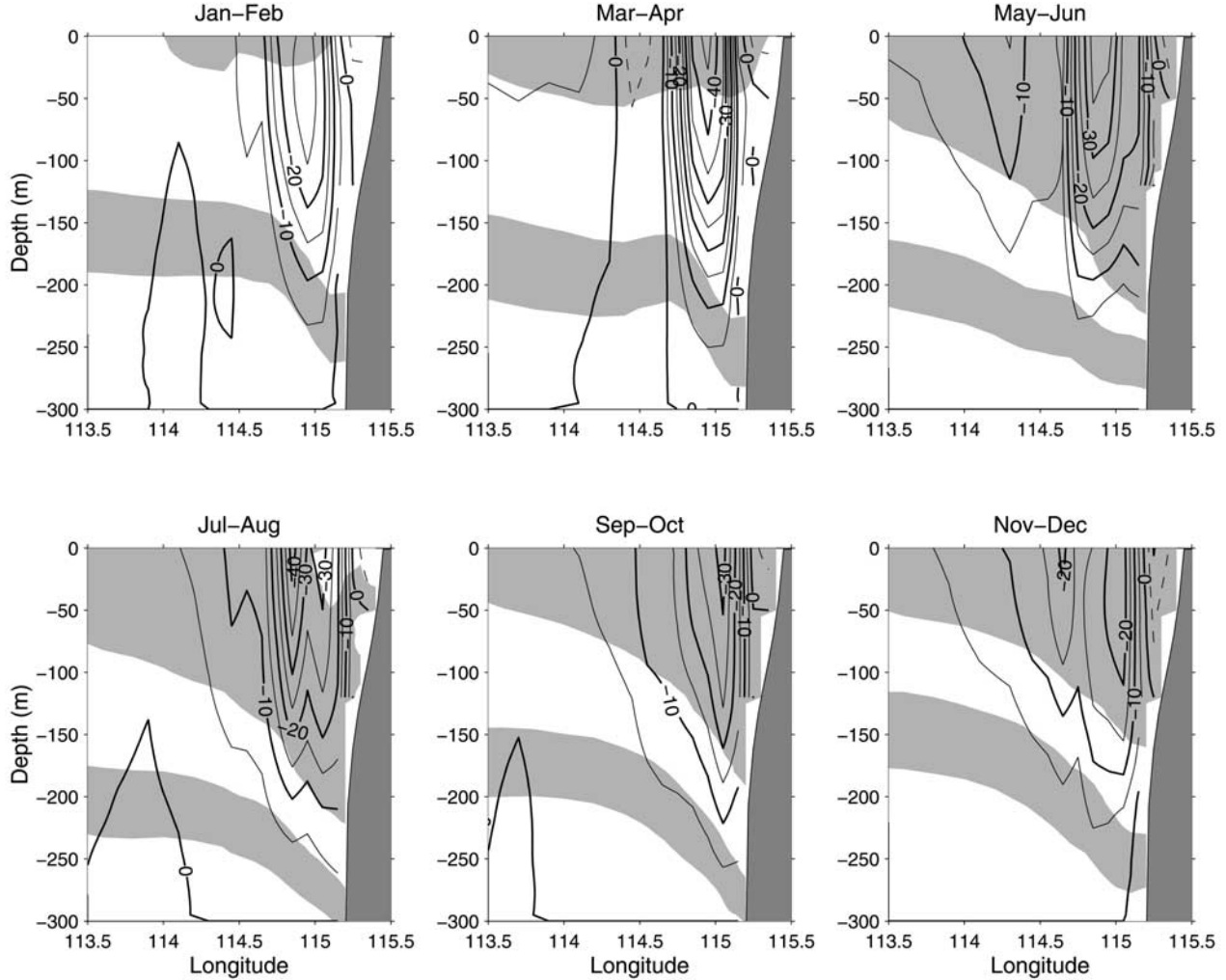


Figure 7. (continued)

stress, the northward Ekman transport peaks in July at 0.6 Sv. Thus both the annual mean and annual variation of the Ekman transport are small compared with the geostrophic transport.

[29] Figure 8 further shows the annual cycle of the maximum southward current velocity. Note that during the summer months when the northward wind stress is strong, the maximum velocity is located at depths of 30–40 m (not shown), although it is only marginally faster than the surface velocity. Southward velocity peaks during April–May at $55\text{--}56 \text{ cm s}^{-1}$, 2 months earlier than the maximum volume transport. The maximum velocity drops to about 40 cm s^{-1} in June, recovers a little in July and then decreases steadily in the later half of the year.

[30] The seasonality of the Leewin Current is further demonstrated by the amplitude and phase of the temperature annual harmonics (Figure 9). The largest temperature amplitude of $1.4^\circ\text{--}1.6^\circ\text{C}$ is near the surface. However, dynamically more important, the temperature amplitude at the depth of 100–250 m is larger than 1°C in the Leewin Current immediately off the continental slope, and the magnitude decreases with depth and in the offshore direction (Figure 9). Thus the subsurface annual variation is coastally trapped. Below 100 m, the temperature maximum

occurs in June–July east of 113°E and lags in the offshore direction, occurring in September at 110°E .

4.4. Fremantle Sea Level and Inshore Dynamic Height

[31] Here we examine the annual variation of the Fremantle sea level and its relationship with the surface dynamic height inshore of the Leewin Current. The Fremantle sea level deviation has an annual range of 23 cm, peaking in June (Figure 10), which is slightly higher than the annual range of 20 cm without the inverted barometric correction [Pattiaratchi and Buchan, 1991]. The sea surface dynamic height ($\zeta_{0,300}$) at 32°S , 115.4°E on the inshore edge has an annual range of nearly 20 cm. Its annual cycle is very close to that of the Fremantle sea level deviation. Slightly offshore, the dynamic height deviation at 115.2°E has a reduced annual range of 15 cm, 65% of the Fremantle sea level deviation. It tends to lead the Fremantle sea level by less than one month, highest between May and June and lowest between November and December.

[32] The close comparison between $\zeta_{0,300}$ at the inshore edge of the current and the Fremantle sea level deviation indicates that the annual Fremantle sea level variation is strongly related to the sea level variability at the inshore edge of the Leewin Current. The very weak secondary peak of



Figure 8. (top) Monthly geostrophic volume transport referenced to 300 m and the Ekman transport east of 110°E along 32°S. Negative transport is southward. (bottom) Annual cycle of maximum southward velocity along 32°S.

the dynamic height in October indicates a weak semi-annual variation [Morrow and Birol, 1998]. At the offshore boundary of the Leeuwin Current (111.5°E as shown), the surface dynamic height variation is much weaker (Figure 10).

[33] In summary, the subsurface annual variation of the Leeuwin Current is coastally trapped at 32°S. Sea level variations associated with strength of the current occur almost exclusively at the inshore side of the current. Thus, the Leeuwin Current can be represented by its inshore dynamic height (Appendix A), which is closely linked with the Fremantle sea level. The high (low) sea level at Fremantle during winter (summer) is indicative of a strong (weak) Leeuwin Current. The sea level variation of 23 cm corresponds to a transport variation of 2.9 Sv.

5. Interannual Variability

[34] In this section, we analyze the interannual variations of the Leeuwin Current and Fremantle sea level. In section 5.1, we present the ENSO composites of the SOI and Fremantle SLA; in section 5.2, we present the temperature composites during El Niño and La Niña years based on the Fremantle SLA composites and the temperature gradient relative to the SLA; and in section 5.3 we link the Leeuwin Current variation with the Fremantle sea level deviation and derive a linear relationship between the sea level deviation and the Leeuwin Current geostrophic trans-

port on annual and interannual timescales. Note that similar conclusions can be derived by using the temperature gradient relative to the SOI to construct the temperature composites as tested in Appendix B3.

5.1. SOI and SLA Composites

[35] On the basis of the annual mean SOI and taking into account the influence of the regime shift on the SOI [Gershunov and Barnett, 1998], 11 El Niño years and 12 La Niña years are identified from 1950 to 2000 (Table 2; Figure 11). Most El Niño years have lower than normal annual mean Fremantle SLA, while most La Niña years have the opposite (Figure 11).

[36] The SOI and Fremantle SLA composites during the El Niño and La Niña years are constructed by averaging the SOI and the Fremantle SLA over the respective years listed in Table 2. The SOI composite during an El Niño year, $SOI_{ElNiño}$, has small values during the early months, reaches maximum negative values of -12 to -14 in the winter months, and then slowly reduces to less than -10 in December (Figure 12). The SOI composite in a La Niña year, $SOI_{LaNiña}$, has two peaks in April and October of 10 and 11.6, respectively. The annual mean Fremantle SLA is 5.6 cm higher than the long-term mean during a La Niña year, compared to 3.4 cm lower during an El Niño year (Figure 12). The annual SLA variations, $SLA_{ElNiño}$ and $SLA_{LaNiña}$, have peak values around September, and secondary peaks during the first half of the year. This might be an indication of the interannual variations of the semi-annual signal in the sea level.

5.2. Temperature Composites

[37] Before we analyze the temperature composites, we first show a time series (1988–2000) of the temperature and surface dynamic height at 31.6°S, 114.5°E (Figure 13), which is taken from an optimally interpolated product along a commercial shipping line [Meyers and Pigot, 1999]. Linear interpolation is used to fill data gaps. There are five El Niño years and four La Niña years during this time period (Table 2). Qualitatively, sea surface temperature is slightly higher (also shown by Pearce and Phillips [1988]) and mixed layer and thermocline depths are deeper during a La Niña year, while the opposites occur during an El Niño year, consistent with observations at 26°S [Meyers, 1996]. Despite mesoscale variability related to the Leeuwin Current [Pearce and Griffiths, 1991] and the distance between this location and Fremantle, the annual and interannual variations of the surface dynamic height at 31.6°S, 114.5°E referenced to 300 m and the Fremantle sea level compare well (Figure 13). The dynamic height tends to lead the Fremantle sea level variation by one month or so during most years.

[38] There is not enough data to document the interannual variability of the Leeuwin Current along 32°S. Instead, we use composite averages based on parameters obtained in section 3. The temperature composites during the El Niño and La Niña years are calculated by adding the monthly temperature climatology and a composite anomaly, which is the product of the Fremantle SLA composite and the temperature gradient relative to SLA,

$$T_{ElNiño}(x, z, d) = T_{C0} + T_{SLA}(x, z, d) \times SLA_{ElNiño}(d),$$

$$T_{LaNiña}(x, z, d) = T_{C0} + T_{SLA}(x, z, d) \times SLA_{LaNiña}(d).$$

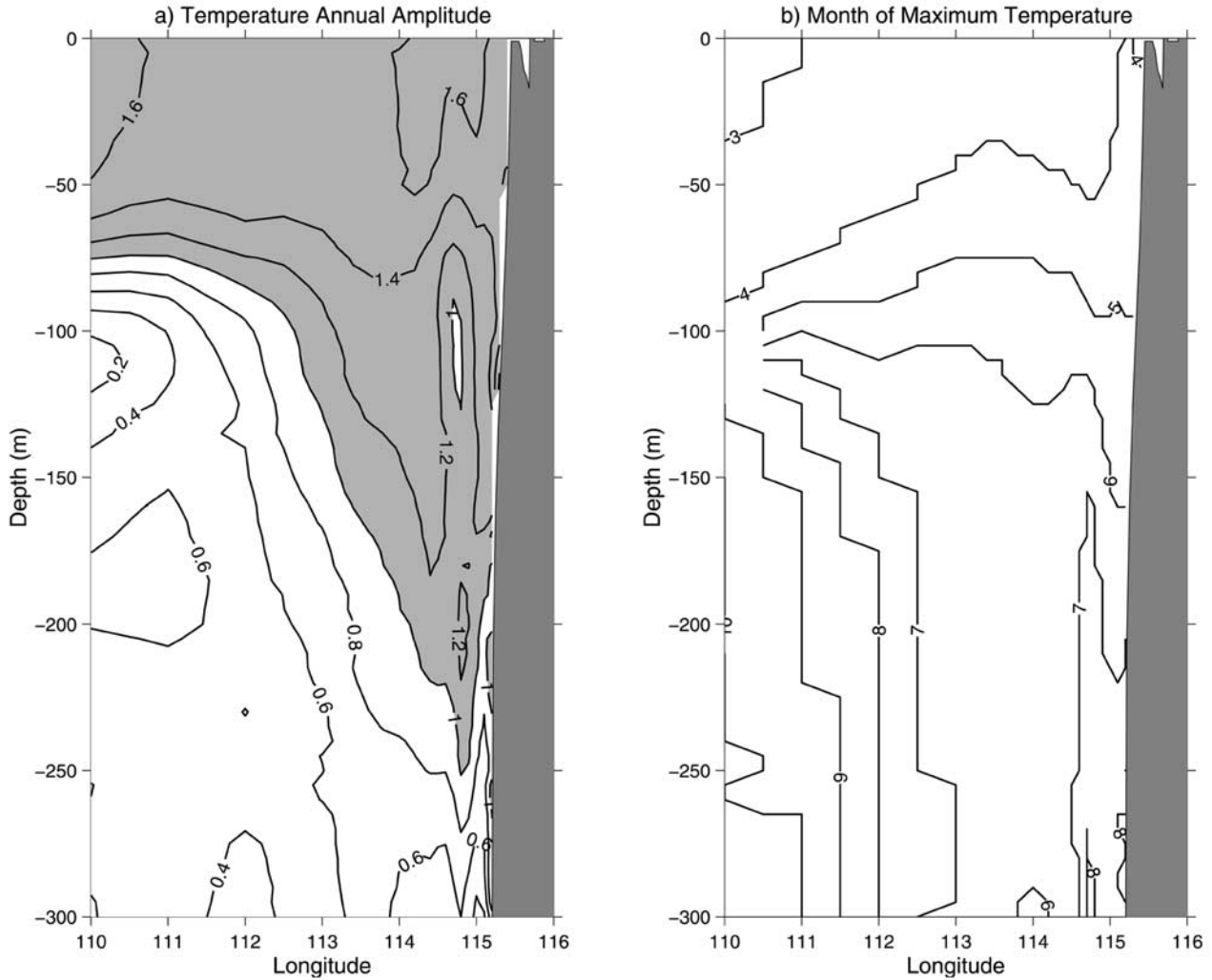


Figure 9. (a) Amplitude and (b) phase of the annual harmonic of the climatology temperature along 32°S. The phase is denoted by the month of maximum temperature.

The salinity is calculated from the monthly T-S relationship. [39] The annual mean composite anomalies are presented in Figure 14. In the Leeuwin Current region, the annual mean temperature anomaly is positive during a La Niña year and negative during an El Niño year, with peak values of 0.8°C and -0.4°C at 200–300 m depth adjacent to the upper continental slope. The anomalies weaken to <0.1°C offshore. Thus, like the annual variation, the ENSO related Leeuwin Current variability is also coastally trapped.

5.3. Fremantle Sea Level Deviation and the Leeuwin Current

[40] In this section, we first compare the inshore surface dynamic height of the Leeuwin Current with the Fremantle sea level in the ENSO composites, and then provide a linkage between the Fremantle sea level and the Leeuwin Current transport using a linear regression.

[41] Variations of the Fremantle sea level and the surface dynamic height at the inshore edge of the Leeuwin Current are similar in their El Niño and La Niña composites

(Figure 15). The annual mean dynamic height at the eastern-most grid point, 115.4°E, is 2.6 cm lower during an El Niño year than the climatology, while it is 5.0 cm higher during a La Niña year. These are about 80% of the Fremantle SLA variations.

[42] The annual mean volume transport decreases to 3.0 Sv during an El Niño year, while it increases to 4.2 Sv during a La Niña year, compared to the climatology mean of 3.4 Sv (Figure 16). The annual phases of volume transport during the El Niño and La Niña years are similar to the mean climatology (Figure 16, top).

[43] In a reduced gravity model (Appendix A), there is a quadratic relationship between the Leeuwin Current volume transport and the surface dynamic height difference across the current. Since the offshore dynamic signals are weak, the inshore surface dynamic height, or the Fremantle sea level, can be used to represent the dynamic height difference. Linear and quadratic regressions between the volume transport and the Fremantle sea level deviation are calculated by treating the monthly values in the composites as

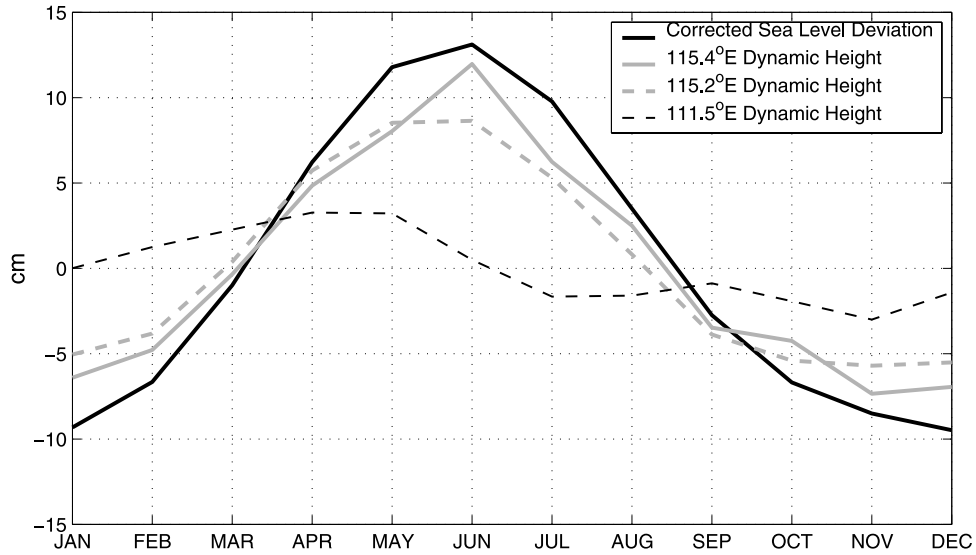


Figure 10. Comparison between the Fremantle sea level deviation and the surface dynamic height deviations referenced to 300 m at 111.5°E , 115.2°E , and 115.4°E .

individual data input (Figure 16, bottom). A linear function is good enough to describe the relationship between the volume transport and the sea level deviation, due to the small range of the latter. From the linear regression relationship, there is a 0.13 Sv change of volume transport for every 1 cm of sea level deviation, that is, the Leeuwin Current volume transport = $3.4 + 0.13 \times (\text{sea level deviation})$ Sv. This justifies and calibrates the usage of the

Fremantle sea level as an index for the strength of the Leeuwin Current.

6. Discussions and Summary

6.1. Offshore Limit of the Leeuwin Current

[44] Since the wind-driven Sverdrup flow is northward at our 32°S section [Tomczak and Godfrey, 1994], the offshore

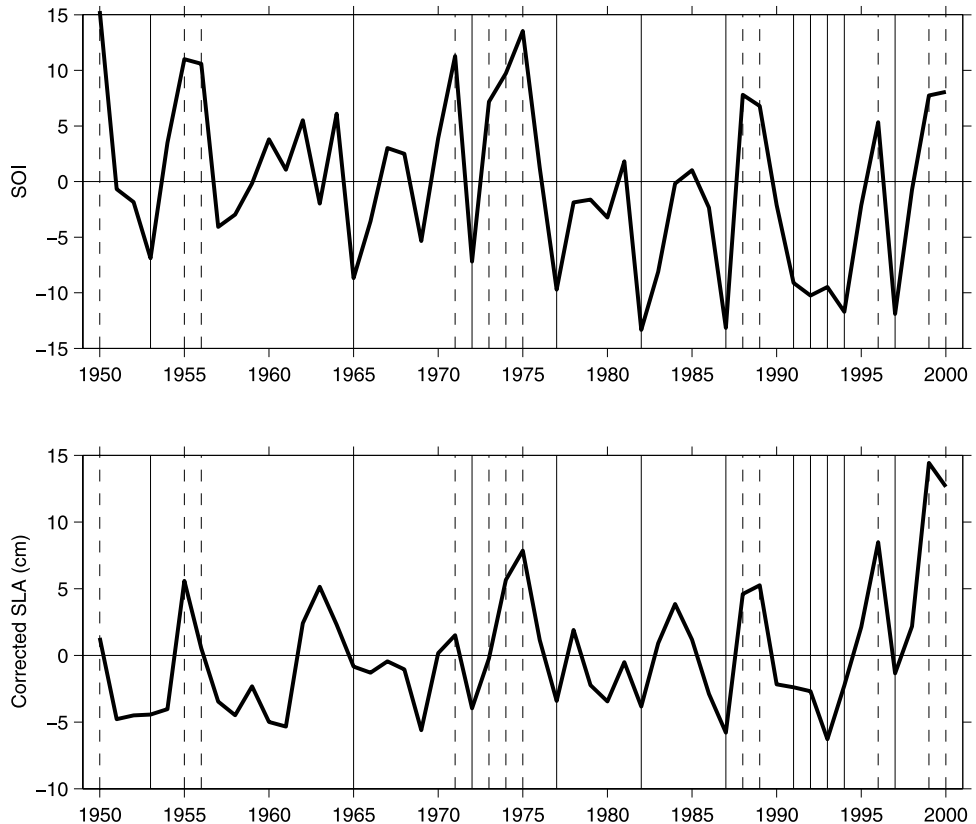


Figure 11. Annual average SOI and Fremantle SLA. The vertical solid lines denote the El Niño years and the dashed lines denote the La Niña years.

Table 2. El Niño and La Niña Years Based on the Annual Mean SOI

	Years
El Niño	1953, 1965, 1972, 1977, 1982, 1987, 1991, 1992, 1993, 1994, 1997
La Niña	1950, 1955, 1956, 1971, 1973, 1974, 1975, 1988, 1989, 1996, 1999, 2000

limit of the Leeuwin Current should be identified by the flattening of isopycnals (S. Godfrey, personal communication, 2003). At 110°E, the isopycnals slightly tilt upward to the west in the annual mean density structure (Figure 6c). Thus a portion of the Leeuwin Current flows southward west of 110°E. When we extend the section to 108°E where the mean isopycnals become almost flat, there is only a 0.3 Sv increment in the southward geostrophic transport in the annual mean, and the annual cycle of the volume transport east of 108°E is similar to that east of 110°E (Figure 17). Thus the bulk of the Leeuwin Current transport and its variation are captured by the flow east of 110°E.

6.2. Dynamics of the Annual and Interannual Variability

[45] In Figure 9b, the offshore phase propagation of the subsurface temperature annual anomaly is consistent with a wind-driven Leeuwin Current annual cycle [McCreary *et al.*, 1986]. The coastal-trapping of the annual temperature variation at 32°S indicates that the local and upstream winds

have an integrated impact. However, it is still necessary to delineate the regional wind effect and the remote Pacific effect on the annual cycle [e.g., Potemra, 2001] by analyzing dynamic balances in spatial data sets and realistic model simulations in future studies.

[46] The peak interannual temperature variation (Figure 14) occurs deeper than that of the maximum amplitude of annual temperature variation (Figure 9). This suggests that the forcing mechanism of the interannual temperature variation is different from that of the annual cycle. A deeper signal indicates that the source of energy is from farther upstream along a characteristic path [Kessler and McCreary, 1993; Wijffels and Meyers, 2003]. Local wind forcing may not be important to the Leeuwin Current variation on the interannual timescale. ENSO signals have been identified in the subsurface temperature at 26°S along the Western Australian coast [Meyers, 1996], and our study shows that these signals can propagate farther south along the coastal waveguide, as seen in the coastal sea levels [Pariwono *et al.*, 1986] (our Figure 2).

[47] On both the annual and interannual timescales, the surface dynamic height in the deep ocean tends to lead the Fremantle sea level variation (Figures 10 and 13). This may be a result of the retardation effect due to bottom friction on the continental shelf, similar to an “ENSO jet” [Clarke and Van Gorder, 1994].

6.3. Surface Isothermal Layer Depth

[48] Ecosystem and fishery research requires information on the variability of the surface isothermal layer depth

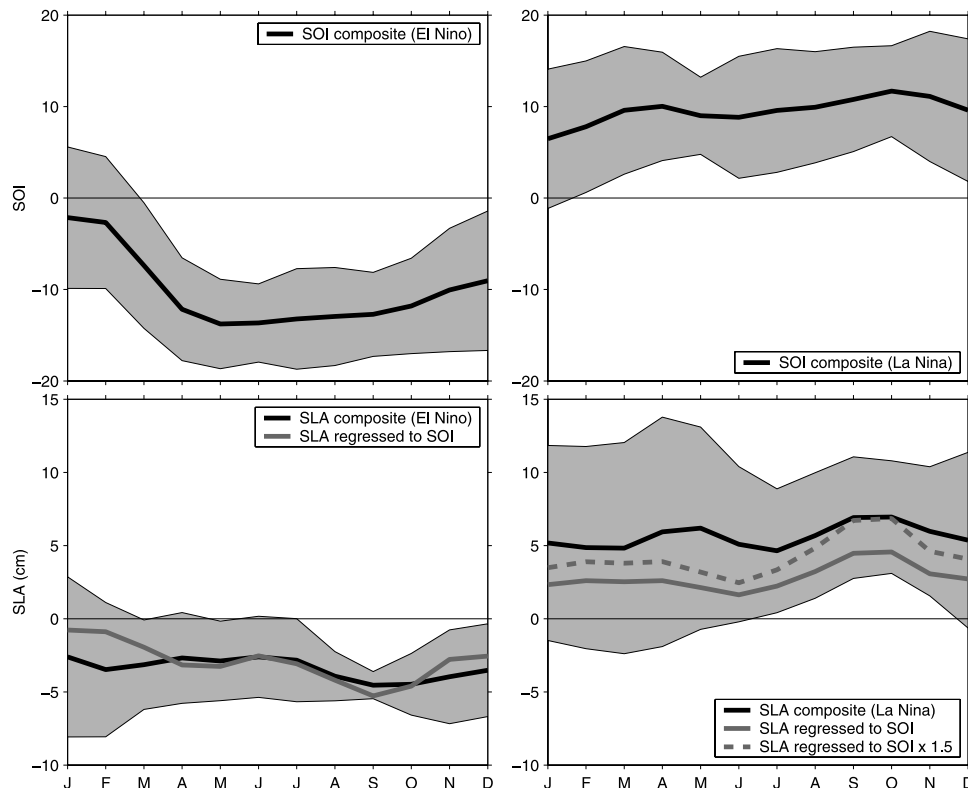


Figure 12. Composites of the SOI and the Fremantle SLA during the 11 El Niño and 12 La Niña years from 1950 to 2000 listed in Table 2. The shadings denote their standard deviations. Also shown are the linear regression results between the SLA and the SOI used in Appendix B3.

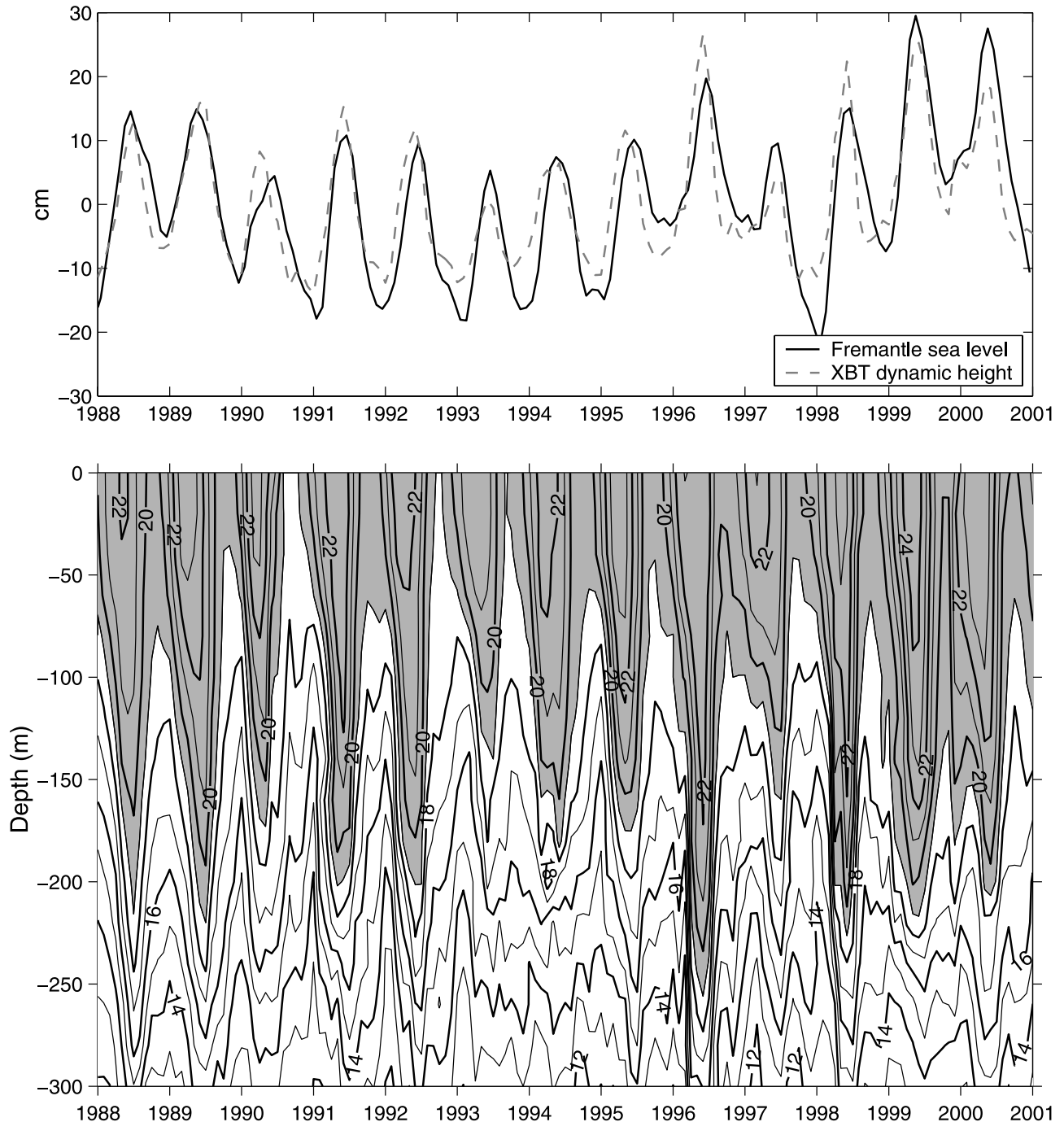


Figure 13. (top) Surface dynamic height deviation and (bottom) upper ocean temperature evolution mapped at 31.6°S, 114.5°E during 1988–2000. The Fremantle sea level deviation is shown in the top panel for comparison.

for the mean seasonal cycle and the ENSO composites (Figure 18). The surface isothermal layer depth is defined as the depth where the temperature is 0.5°C colder than the surface temperature. In the mean annual cycle, the offshore (west of 114°E) isothermal layer is shallower than 40 m during the austral summer and deepens to 60 m during the austral winter (Figure 18, top). The isothermal layer over the slope is deeper in the winter months, due to the Leewin

Current advection, and reaches its maximum depth of 120 m in June.

[49] The El Niño and La Niña composites show that large interannual isothermal layer depth variations occur on the inshore side of the Leewin Current core (Figure 18, bottom). The annual average isothermal layer depth is about 10 m shallower during an El Niño year and about 12 m deeper during a La Niña year on the

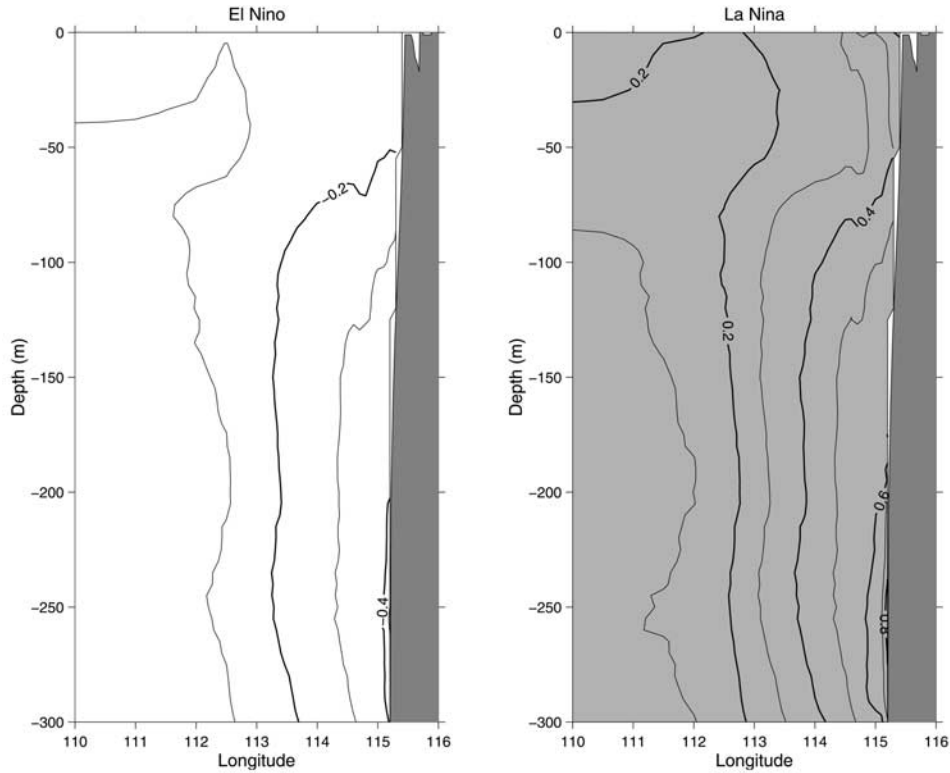


Figure 14. Annual mean temperature anomalies along 32°S during the El Niño and La Niña years. Shading denotes positive anomaly.

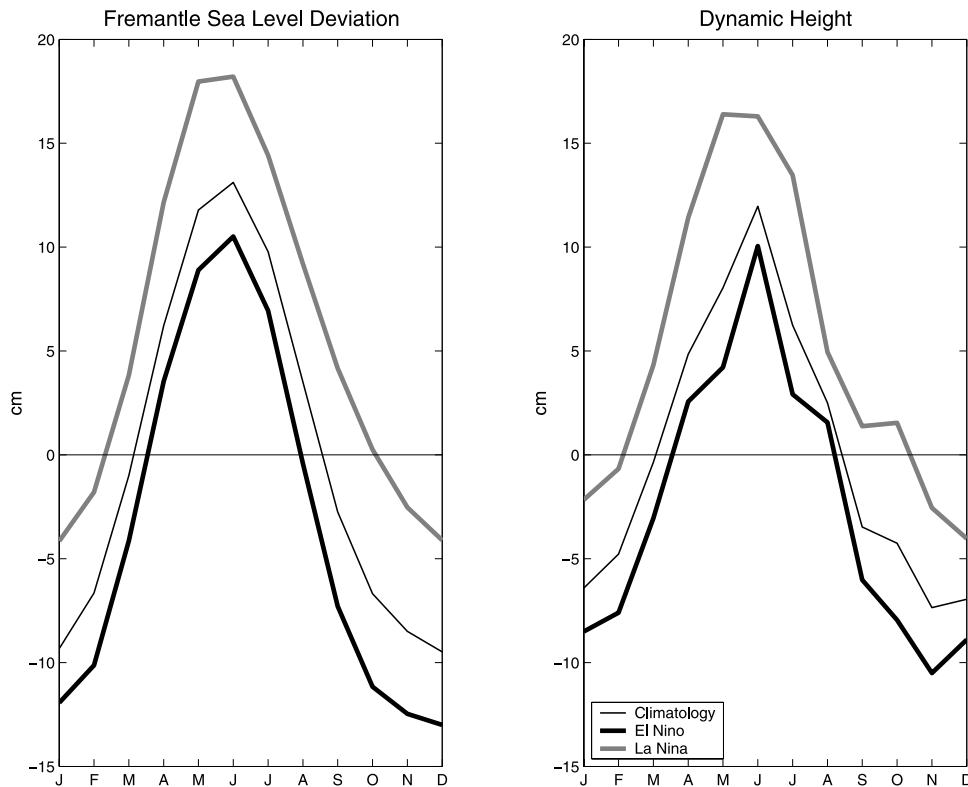


Figure 15. (left) Monthly Fremantle sea level deviation in the climatology and during the El Niño and La Niña years. (right) Surface dynamic height deviations referenced to 300 m at 32°S, 115.4°E in the climatology and during the El Niño and La Niña years.

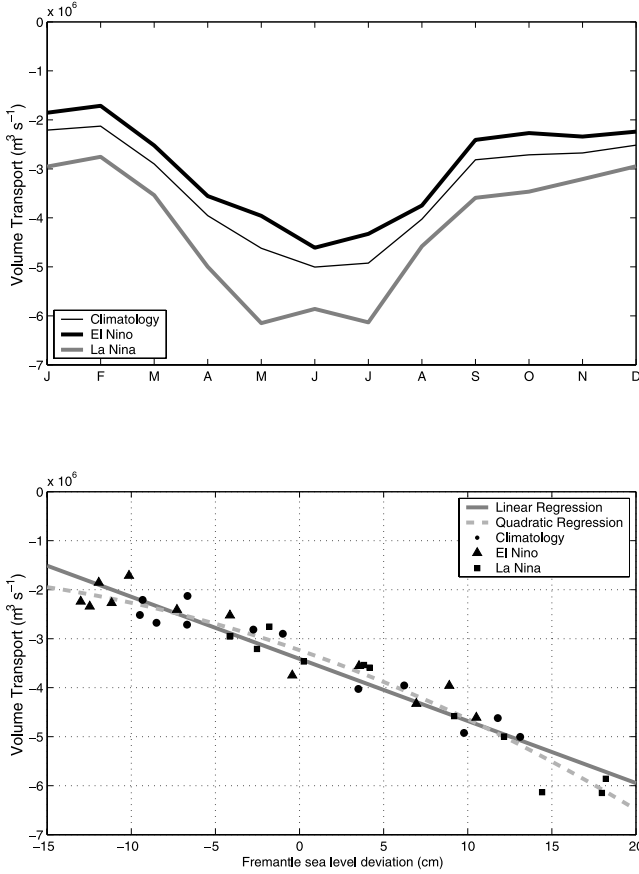


Figure 16. (top) Geostrophic volume transport of the Leeuwin Current referenced to 300 m in the climatology, and in the El Niño and La Niña years. (bottom) Scatterplot between the Fremantle sea level deviation and the geostrophic transport in the climatology, and in the El Niño and La Niña years. The cross-hatched lines are the linear and quadratic regressions between the sea level deviation and the volume transport.

upper continental slope. Near 110°E, there are up to 5-m isothermal layer depth variations in the opposite sign to those on the slope. A shallower offshore mixed layer depth during La Niña years may be important for the

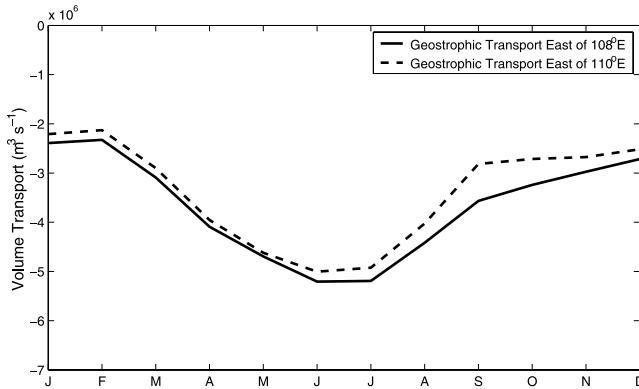


Figure 17. Comparison between the southward geostrophic volume transports referenced to 300 m east of 110°E and that east of 108°E along 32°S.

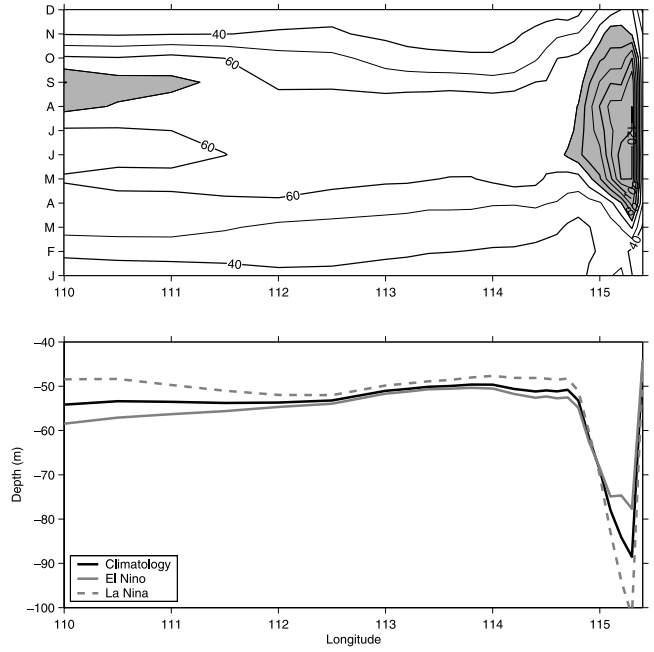


Figure 18. (top) Surface isothermal layer depth (in meters) in the annual climatology and (bottom) annual mean surface isothermal layer depths in different composites along 32°S. The shaded areas in the top panel denote depths greater than 70 m.

higher western rock lobster recruitment during these years.

6.4. Summary

[50] In this paper, we have examined the annual and interannual variations of the Leeuwin Current using a

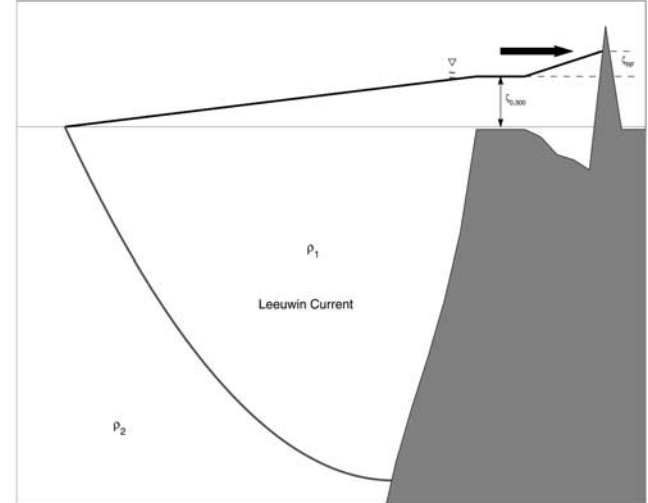


Figure A1. Schematic of the Leeuwin Current in a one-moving-layer reduced gravity model. At the offshore end of the current, the lower layer is outcropped. The arrow above the sea surface denotes the zonal wind stress. The solid line above the sea surface shows the sea level variation across the current, where the definitions of $\zeta_{0,300}$ and ζ_{RF} are denoted.

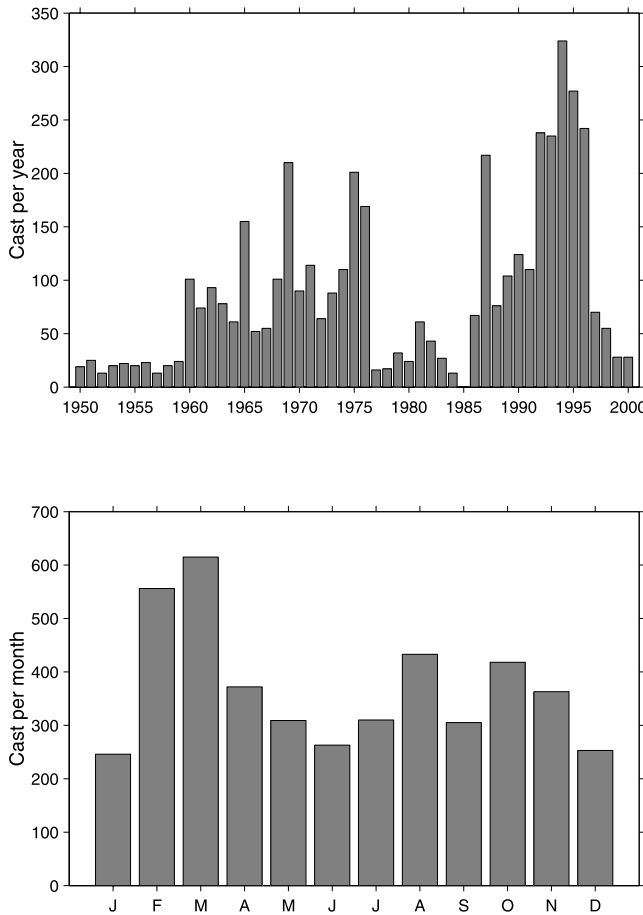


Figure B1. Number of casts (top) per year and (bottom) per month in the upper ocean thermal archive within the region shown in Figure 3.

monthly upper ocean climatology and its El Niño/La Niña composites along 32°S. On the annual timescale, the Leeuwin Current is narrow and weak during the austral summer and broad and strong during the austral winter. The Leeuwin Current attains its maximum southward geostrophic speed of 45 cm s⁻¹ during April–May, while its maximum southward volume transport of 5 Sv occurs in June–July. The annual mean poleward transport east of 110°E is 3.4 Sv. On the interannual timescale, the Leeuwin Current is stronger during a La Niña year and weaker during an El Niño year. The annual mean volume transports during the El Niño and La Niña years are 3.0 and 4.2 Sv, respectively.

[51] Both the annual and interannual dynamic signals in the Leeuwin Current are coastally trapped and the offshore signals are weak. Thus the Leeuwin Current variation is well represented by the inshore sea surface dynamic height. The Fremantle sea level variations on the annual and interannual timescales are consistent with the inshore sea surface dynamic height. A quasi-linear relationship is established between the Fremantle sea level and the Leeuwin Current volume transport: a 0.13-Sv volume transport variation corresponds to every centimeter of the sea level variation. This justifies and calibrates the usage of the

Fremantle sea level as the index of the Leeuwin Current strength.

Appendix A: Dynamic Balance in the Leeuwin Current

[52] In this appendix, we use the zonal momentum equation to derive the geostrophic balance of the Leeuwin Current, and decompose the Fremantle sea level into a major inshore dynamic height component and a minor local wind-driven component. Also, we establish an analytic relationship between the inshore dynamic height and the Leeuwin Current volume transport.

A1. Zonal Momentum Balance in the Leeuwin Current

[53] The zonal momentum equation is written as

$$\frac{\partial u}{\partial t} + u \frac{\partial u}{\partial x} + v \frac{\partial u}{\partial y} + w \frac{\partial u}{\partial z} - fv = -\frac{1}{\rho_0} \frac{\partial p}{\partial x} + \frac{\partial}{\partial x} \left(A_H \frac{\partial u}{\partial x} \right) + \frac{\partial}{\partial y} \left(A_H \frac{\partial u}{\partial y} \right) + \frac{1}{\rho_0} \frac{\partial \tau^x}{\partial z}. \quad (\text{A1})$$

Here x , y , and z are positive eastward, northward, and upward, u , v , w are zonal, meridional, and vertical velocities, $f = -7.7 \times 10^{-5}$ s⁻¹ is the Coriolis parameter at 32°S, $\rho_0 = 1025$ kg m⁻³ is the mean density, and p is the

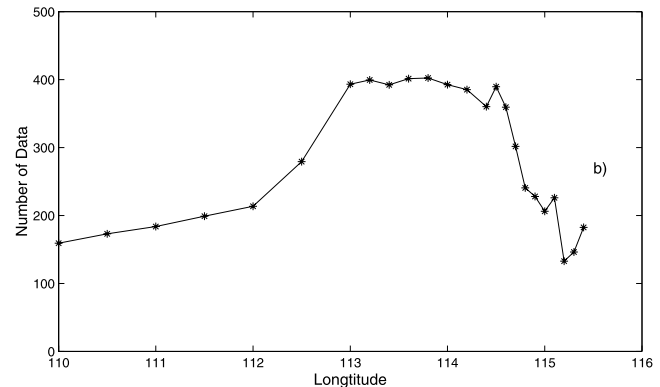
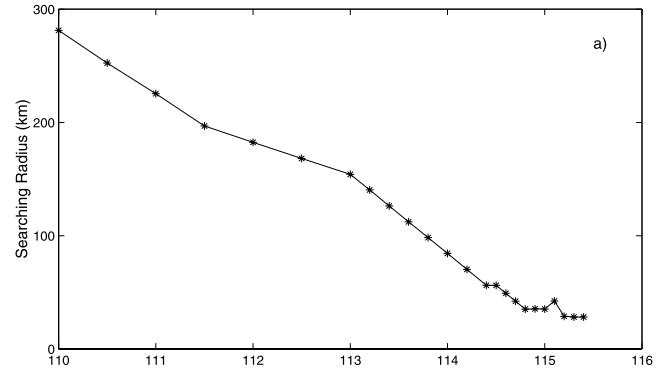


Figure B2. (a) Mean zonal searching radius and (b) average number of data points within the searching radius in the climatology construction along 32°S.

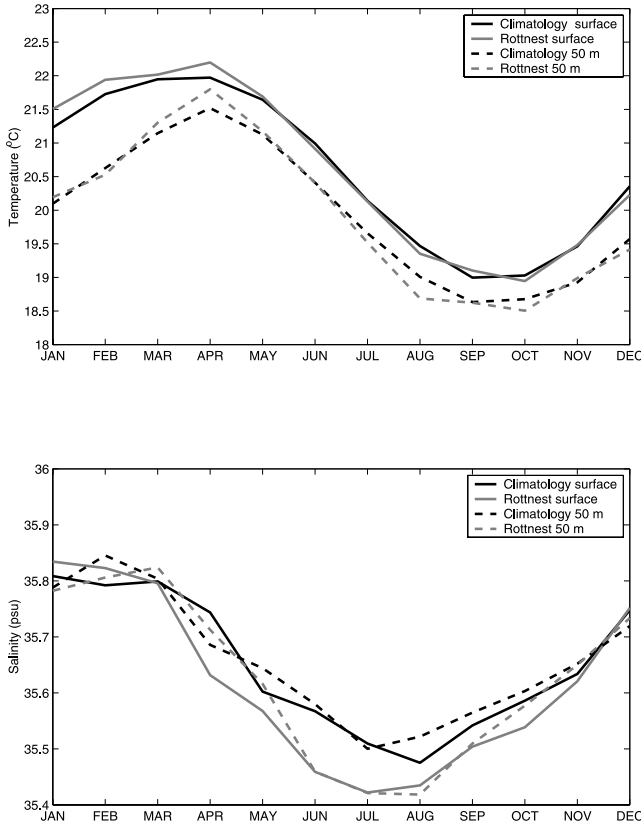


Figure B3. Comparisons between the climatology temperature and salinity at 32°S, 115.4°E and the average annual cycles from the Rottnest station measurements.

pressure. A_H is the horizontal turbulence coefficient and τ^x is the zonal vertical Reynolds stress, and u and v have scales of 0.1 and 0.5 m s⁻¹, respectively [Thompson, 1984]. The vertical velocity scale can be inferred from the continuity relation. Assuming the temporal scale is 1 month and the horizontal scale is 50 km for the Leeuwin Current, the temporal derivative and advection terms on the left-hand side of the equation are all more than a magnitude smaller than the Coriolis term and can be neglected. Away from the coastal boundary, the horizontal turbulent mixing terms on the right-hand side can also be neglected. This results in

$$fv = \frac{1}{\rho_0} \frac{\partial p}{\partial x} - \frac{1}{\rho_0} \frac{\partial \tau^x}{\partial z}. \quad (\text{A2})$$

We define $v = v_G + v_E$, that is, meridional velocity is separated into the geostrophic and Ekman components, where $v_G = 1/(f\rho_0)\partial_p/\partial_x$ and $v_E = -1/(f\rho_0)\partial\tau_x/\partial_z$. The Ekman velocity is much smaller, as in section 4.2.

[54] Inshore of Rottnest Island, the current velocity is essentially zero, so that the momentum balance is written as

$$\frac{1}{\rho_0} \frac{\partial p}{\partial x} = \frac{1}{\rho_0} \frac{\partial \tau^x}{\partial z}. \quad (\text{A3})$$

[55] Assuming the pressure gradient does not vary with depth (barotropic), we can replace p with $\rho_0 g \zeta$. Integrating

vertically, the zonal wind-driven sea level difference between Rottnest Island and Fremantle can be estimated as [Bowden, 1983]

$$\zeta_{RF} = C \tau_0^x \Delta x / g \rho_0 \bar{H}. \quad (\text{A4})$$

Here C is between 1 and 1.5 representing the effect of bottom stress, τ_0^x is the zonal wind stress, Δx is the distance between Fremantle and Rottnest (10 km), g is the gravity constant, ρ_0 is the mean surface density, and \bar{H} is the mean water depth.

[56] From the SOC air-sea flux climatology, the annual variation of the zonal wind stress is 0.16 N m⁻² (Figure 5). Assuming $C = 1$ and $\bar{H} \sim 20$ m, ζ_{RF} has an annual variation of only 1 cm, with the highest value in July (not shown).

A2. Fremantle Sea Level Decomposition

[57] From Appendix A1, the Fremantle sea level can be decomposed as $\zeta_{Fremantle} = \zeta_{Rottnest} + \zeta_{RF}$, where $\zeta_{Rottnest} = \zeta_{0,300} + \zeta_{300}$ is the sea level at the eastern most grid point of our section, 32°S, 115.4°E. Here $\zeta_{0,300}$ is the dynamic height at the sea surface relative to 300 m calculated from the upper ocean climatology, and ζ_{300} is the dynamic height at the reference depth 300 m which cannot be determined from the study and is assumed to have small variation. Thus we use $\zeta_{Rottnest} = \zeta_{0,300}$ in this study. The sea level deviations are obtained by removing the mean values.

[58] In a one-and-a-half layer model with an outcropping interface (Figure A1), the geostrophic volume transport can be expressed as $V_{BC} = g' H_{max}^2 / 2f$, where g' is the reduced gravity and H_{max} is the maximum depth of the upper layer on the non-outcropping side of the current [McClamans et al., 1999]. The surface elevation at the non-outcropping side of the current can be expressed as $\zeta_{BC} = g' H_{max} / g$. This gives

$$V_{BC} = g^2 \zeta_{BC}^2 / 2g' f. \quad (\text{A5})$$

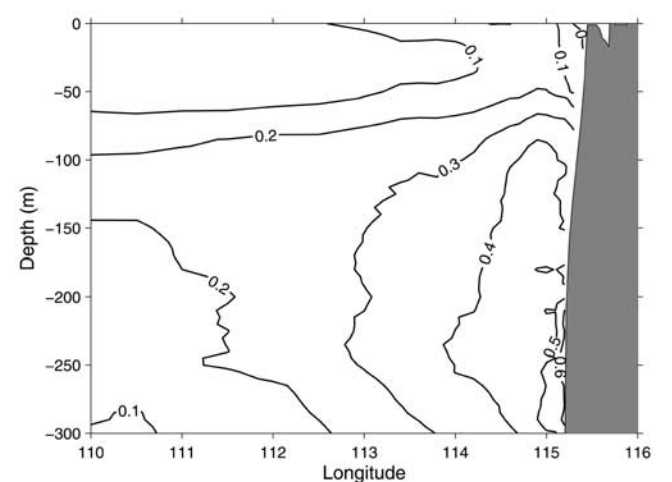


Figure B4. Annual average of the temperature gradient against the SOI, calculated by replacing the SLA with the SOI in the temperature fitting. The unit is °C per 10 SOI units.

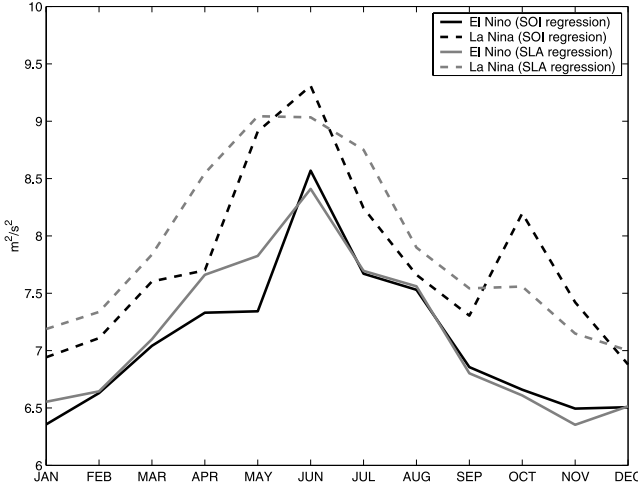


Figure B5. Comparison between the surface dynamic heights at 115.4°E by using regression coefficients to the Fremantle SLA and using regression coefficients to the SOI in the El Niño and La Niña years.

[59] In the case of the Leeuwin Current, the inshore side can be regarded as the non-outcropping side because of the small offshore variations. The inshore dynamic height $\zeta_{0,300}$ can be used for ζ_{BC} in equation (A5). That is, there is a

quadratic relationship between the baroclinic volume transport of the Leeuwin Current, V_{BC} , and the baroclinic sea surface elevation $\zeta_{0,300}$.

Appendix B: Validation and Sensitivity Tests of Temperature Fitting

[60] In this appendix, we first introduce some statistics from the temperature fitting, and then validate the annual climatology using the Rottnest station data. Finally, we carry out a number of sensitivity tests on the temperature fitting.

B1. Fitting Statistics

[61] Figure B1 shows the data density at the sea surface by year and by month in the upper ocean thermal archive off Fremantle. Note that the data density decreases with depth because the majority of the data are near-surface casts (not shown). The data density is low during the 1950s and late 1970s to early 1980s. The low data density after 1997 is due to a delay in data archiving. Overall there are more than 200 casts in each month, the highest number of profiles is in February and March (Figure B1). Figure B2 shows the averaging zonal searching radius in the climatology fit, which ranges from about 280 km to about 25 km, equal to or slightly larger than the pre-assigned minimum searching radius.

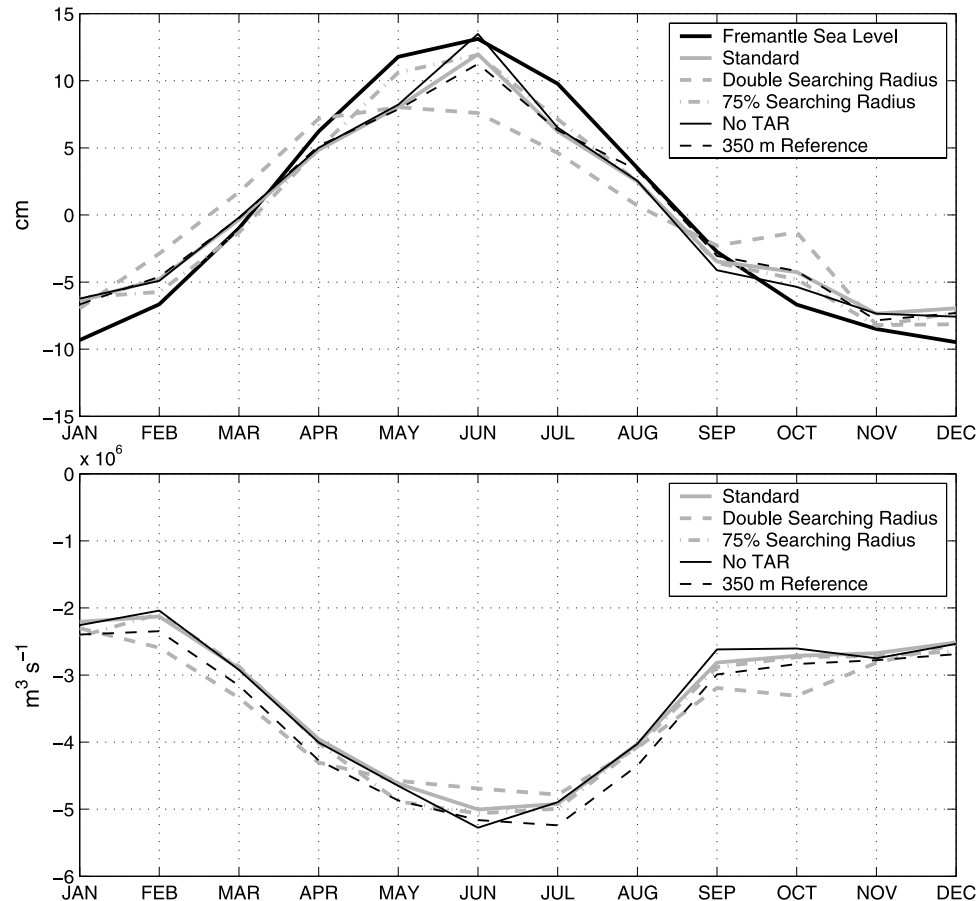


Figure B6. (top) Comparison between the annual Fremantle sea level deviation and the surface dynamic height deviations at 115.4°E in the standard case and four sensitivity test cases listed in Table B1. (bottom) Geostrophic volume transports in the different cases.

Table B1. Annual Range of the Surface Dynamic Height Variation at 115.4°E (cm) and the Leeuwin Current Volume Transport (Sv) in the Standard Case and the Four Test Cases

	Standard	Double R	75% R	No TAR	350 m
Dynamic height variation range	19	16	20	21	19
Mean volume transport	3.4	3.5	3.4	3.4	3.6

On average there are more than 100 data points for each fit (Figure B2).

B2. Validation With Rottnest Station Data

[62] The mean annual cycle from the Rottnest station measurements, which are not included in the upper ocean thermal archive, are compared with the annual cycle of climatology at the eastern most grid point, 32°S, 115.4°E, as an independent check of the climatology (Figure B3). The difference between the surface and bottom (50 m) temperatures (both of which peak in March–April) indicates that weak temperature stratification exists all year-round. There is only weak salinity stratification (Figure B3). The climatological temperatures are consistent with the Rottnest station data on the annual cycle, but the climatological T-S relationship underestimates the salinity minimum during austral winter by almost 0.1 psu.

B3. Sensitivity Analysis

[63] We first use the SOI to replace the Fremantle SLA in the temperature fitting. The annual average of the temperature gradient against the SOI is very similar to that against the Fremantle SLA as presented in Figure 14 (Figure B4). Using the temperature gradient against the SOI, we can also derive the temperature anomalies and temperature composites in El Niño and La Niña years. Here we have increased the La Niña anomaly by 50% to take into account the nonlinear climate shift effect (see below). The annual surface dynamic heights at the inshore grid are similar to those derived in section 5 (Figure B5). Thus the ENSO composites derived from the regression coefficients against the Fremantle SLA would be derived similarly from the regression coefficients against the SOI, but we avoid the nonlinearity due to the climate regime shift.

[64] The nonlinearity between the SOI and the Fremantle SLA is quantified as follows. We compute the linear regression, $SLA(d) = c_0(d) \times SOI(d)$, between the Fremantle SLA and the SOI in each month. The product of the SOI composite and the regression coefficient, $c_0(d) \times SOI_{ElNi\tilde{n}o}(d)$, compares well with the Fremantle SLA composite during an El Niño year, while $c_0(d) \times SOI_{LaNi\tilde{n}a}(d)$ underestimates the Fremantle SLA magnitude during a La Niña year and it needs a factor of 1.5 to match with the SLA composite (Figure 12). This is due to the fact that the SOI has declined since the regime shift in 1977.

[65] Further, we test the sensitivity of our results (called the standard case) by changing the fitting parameters. Four tests are carried out: (1) doubling the preset spatial searching radii; (2) reducing the preset spatial search radii by 25%; (3) removing the topographic adjusted relief (TAR) in the weighting function; and (4) using 350 m as the reference depth. The annual variations of the surface dynamic height at 115.4°E and the total volume transport are presented for the comparison (Figure B6).

[66] When doubling the spatial searching radius, there is a reduced annual range of the inshore dynamic height deviation and the peak is shifted to May (Figure B6; Table B1). There tends to be an obvious secondary peak in October. Similar changes are present in the volume transport. When reducing the searching radius by 25%, it gives the closest comparison between the surface dynamic height deviation at 115.4°E and the Fremantle sea level deviations on the annual timescale, but with little effect on the volume transport. Thus the conclusions from this study are not very sensitive to the searching radius selection.

[67] Including and not including the TAR function do not affect the results significantly (Figure B6; Table B1). This suggests that the aliasing between data in the shallow continental shelf and the deep ocean is not critical for this study, because the data density is relatively high despite the narrow continental shelf and slope.

[68] There is almost no change in the annual cycle of the surface dynamic height variation at 115.4°E referenced to 350 m compared with that referenced to 300 m, while the volume transport increases only slightly during most months (Figure B6; Table B1). This confirms that the geostrophic calculation in this region is not very sensitive to the selection of the reference depth, likely due to weak density stratification at 300 m.

[69] **Acknowledgments.** This work is supported by the Strategic Research Fund for the Marine Environment and CSIRO Marine Research. We would like to thank Ann Gronell for processing the upper ocean thermal data, and Jeff Dunn for providing the temperature-salinity relationship. We thank Stuart Godfrey, David Griffin, Chari Pattiarchi, and Tony Koslow for valuable discussions. We also appreciate the helpful comments from John Toole, the editor, and two reviewers.

References

- Battean, M. L., and M. J. Rutherford, Modeling studies of eddies in the Leeuwin Current: The role of thermal forcing, *J. Phys. Oceanogr.*, 20, 1484–1520, 1990.
- Bowden, K. F., *Physical Oceanography of Coastal Waters*, 302 pp., Ellis Horwood, Chichester, England, 1983.
- Caputi, N., C. F. Chubb, and R. S. Brown, Relationship between spawning stock, environment, recruitment and fishing effort for the western rock lobster, *Panulirus Cygnus*, fishery in Western Australia, *Crustaceana*, 68, 213–226, 1995.
- Clarke, A. J., and X. Liu, Interannual sea level in the northern and eastern Indian Ocean, *J. Phys. Oceanogr.*, 24, 1224–1235, 1994.
- Clarke, A. J., and S. Van Gorder, On ENSO coastal currents and sea levels, *J. Phys. Oceanogr.*, 24, 661–679, 1994.
- Cleveland, W. S., and S. J. Devlin, Locally weighted regression: An approach to regression analysis by local fitting, *J. Am. Stat. Assoc.*, 83, 596–610, 1988.
- Cresswell, G. R., and T. J. Golding, Observations of a south-flowing current in the southeastern Indian Ocean, *Deep Sea Res.*, 27, 449–466, 1980.
- Cresswell, G. R., F. M. Boland, J. L. Peterson, and G. S. Wells, Continental shelf currents near the Abrolhos Islands, Western Australia, *Aust. J. Mar. Freshwater Res.*, 40, 113–128, 1989.
- D'Adamo, N., Exchange and mixing in Cockburn Sound, Western Australia: A seasonally stratified, micro-tidal, semi-enclosed coastal embayment, Ph.D. thesis, Dep. of Civ. Eng., Univ. of Canterbury, Christchurch, N. Z., Australia, December 2002.
- Dunn, J. R., and K. R. Ridgway, Mapping ocean properties in regions of complex topography, *Deep-Sea Research I*, 49, 591–604, 2002.
- Feng, M., and S. Wijffels, Intraseasonal variability in the South Equatorial Current of the East Indian Ocean, *J. Phys. Oceanogr.*, 32, 265–277, 2002.
- Gershunov, A., and T. P. Barnett, Interdecadal modulation of ENSO teleconnections, *Bull. Am. Meteorol. Soc.*, 79, 2715–2726, 1998.
- Godfrey, J. S., and K. R. Ridgway, The large-scale environment of the poleward-flowing Leeuwin Current, Western Australia: Longshore steric height gradients, wind stresses, and geostrophic flow, *J. Phys. Oceanogr.*, 15, 481–495, 1985.

- Griffin, D. A., J. L. Wilkin, C. F. Chubb, A. F. Pearce, and N. Caputi, Ocean currents and larval phase of Australian western rock lobster, *Panulirus Cygnus*, *Mar. Freshwater Res.*, **52**, 1187–1199, 2001.
- Josey, S. A., E. C. Kent, and P. K. Taylor, New insights into the ocean heat budget closure problem from analysis of the SOC air-sea flux climatology, *J. Clim.*, **12**, 2856–2880, 1999.
- Kalnay, E., et al., The NCEP/NCAR 40-year reanalysis project, *Bull. Am. Meteorol. Soc.*, **77**, 437–471, 1996.
- Kessler, W. S., and J. P. McCreary, The annual wind-driven Rossby wave in the subthermocline equatorial Pacific, *J. Phys. Oceanogr.*, **23**, 1192–1207, 1993.
- Kundu, P. K., and J. P. McCreary, On the dynamics of the throughflow from the Pacific into the Indian Ocean, *J. Phys. Oceanogr.*, **16**, 2191–2198, 1986.
- Levitus, S., and T. P. Boyer, *World Ocean Atlas 1994*, volume 4, *Temperature*, NOAA Atlas NESDIS 4, 117 pp., Natl. Oceanic and Atmos. Admin., Silver Spring, Md., 1994.
- McClimans, T. A., B. O. Johannessen, and T. Jenserud, Monitoring a shelf edge current using bottom pressures or coastal sea-level data, *Cont. Shelf Res.*, **19**, 1265–1283, 1999.
- McCreary, J. P., S. R. Shetye, and P. K. Kundu, Thermohaline forcing of eastern boundary currents, with application to the circulation off the west coast of Australia, *J. Mar. Res.*, **44**, 71–92, 1986.
- Meyers, G., Variation of Indonesian throughflow and the El Niño-Southern Oscillation, *J. Geophys. Res.*, **101**, 12,255–12,263, 1996.
- Meyers, G., and L. Pigot, Analysis of frequently repeated XBT lines in the Indian Ocean, *CSIRO Mar. Lab. Rep.* 238, 43 pp., CSIRO Mar. Res., Hobart, Australia, 1999.
- Meyers, G., R. J. Bailey, and A. P. Worby, Geostrophic transport of the Indonesian throughflow, *Deep Sea Res., Part I*, **42**, 1163–1174, 1995.
- Morrow, R., and F. Birol, Variability in the southeast Indian Ocean from altimetry: Forcing mechanisms for the Leeuwin Current, *J. Geophys. Res.*, **103**, 18,529–18,544, 1998.
- Nitta, T., and S. Yamada, Recent warming of tropical sea surface temperature and its relationship to the Northern Hemisphere circulation, *J. Meteorol. Soc. Jpn.*, **67**, 375–383, 1989.
- Pariwono, J. I., J. A. T. Bye, and G. W. Lennon, Long-period variations of sea level in Australia, *Geophys. J. R. Astron. Soc.*, **87**, 43–54, 1986.
- Pattiaratchi, C. B., and S. J. Buchan, Implications of long-term climate change for the Leeuwin Current, *J. R. Soc. West. Aust.*, **74**, 133–140, 1991.
- Pearce, A. F., Eastern boundary currents of the southern hemisphere, *J. R. Soc. West. Aust.*, **74**, 35–45, 1991.
- Pearce, A. F., and R. W. Griffiths, The mesoscale structure of the Leeuwin Current: A comparison of laboratory model and satellite images, *J. Geophys. Res.*, **96**, 16,730–16,757, 1991.
- Pearce, A. F., and C. B. Pattiaratchi, The Capes current: A summer counter-current flowing past Cape Leeuwin and Cape Naturaliste, southwestern Australia, *Cont. Shelf Res.*, **19**, 401–420, 1999.
- Pearce, A. F., and B. F. Phillips, ENSO events, the Leeuwin Current and larval recruitment of the western rock lobster, *J. Cons. Cons. Int. Explor. Mer.*, **45**, 13–21, 1988.
- Potemra, J. T., Contribution of equatorial Pacific winds to southern tropical Indian Ocean Rossby waves, *J. Geophys. Res.*, **106**, 2407–2422, 2001.
- Reid, J. L., and A. W. Mantyla, The effect of the geostrophic flow upon coastal sea elevations in the northern North Pacific Ocean, *J. Geophys. Res.*, **81**, 3100–3110, 1976.
- Rochford, D. J., Coastal monitoring network, in *CSIRO at Sea-50 years of Marine Science*, edited by V. Mawson, D. J. Tranter, and A. F. Pearce, pp. 49–50, Commonwealth Sci. and Indust. Res. Org., Hobart, Tasmania, Australia, 1988.
- Smith, R. L., A. Huyer, J. S. Godfrey, and J. Church, The Leeuwin Current off Western Australia, 1986–1987, *J. Phys. Oceanogr.*, **21**, 323–345, 1991.
- Smith, W. H., and D. T. Sandwell, Global sea floor topography from satellite altimetry and ship depth soundings, *Science*, **277**(5334), 1956–1962, 1997.
- Thompson, R. O. R. Y., Observations of the Leeuwin Current off Western Australia, *J. Phys. Oceanogr.*, **14**, 623–628, 1984.
- Thompson, R. O. R. Y., Continental-shelf-scale model of Leeuwin Current, *J. Mar. Res.*, **45**, 813–827, 1987.
- Tomczak, M., and J. S. Godfrey, *Regional Oceanography: An Introduction*, 422 pp., Pergamon, New York, 1994.
- Weaver, A. J., and J. H. Middleton, On the dynamics of the Leeuwin Current, *J. Phys. Oceanogr.*, **19**, 626–648, 1989.
- Wessel, P., and W. H. F. Smith, A global self-consistent, hierarchical, high-resolution shoreline database, *J. Geophys. Res.*, **101**, 8741–8743, 1996.
- Wijffels, S., and G. Meyers, An intersection of oceanic wave guides: Variability in the Indonesian Throughflow, *J. Phys. Oceanogr.*, in press, 2003.
- Xie, P., and P. A. Arkin, Global precipitation: A 17-year monthly analysis based on gauge observations, satellite estimates, and numerical model outputs, *Bull. Am. Meteorol. Soc.*, **78**, 2539–2558, 1997.

M. Feng and A. Pearce, CSIRO Marine Research, Underwood Avenue, Floreat, Western Australia 6014, Australia. (ming.feng@marine.csiro.au)

G. Meyers and S. Wijffels, CSIRO Marine Research, Castray Esplanade, Hobart, Tasmania 7000, Australia.